JOURNAL OF PETROLOGY

Journal of Petrology, 2020, 1–24
doi: 10.1093/petrology/egaa068
Advance Access Publication Date: 29 June 2020
Original Article

OXFORD

Trace Element and Isotopic Evidence for Recycled Lithosphere from Basalts from 48 to 53°E, Southwest Indian Ridge

Jixin Wang[1,2], Huaiyang Zhou[1,*], Vincent J. M. Salters[3], Henry J. B. Dick[1,4], Jared J. Standish[4,†] and Conghui Wang[1]

[1]State Key Laboratory of Marine Geology, Tongji University, Shanghai 200092, China; [2]Center of Deep Sea Research, Institute of Oceanology, Chinese Academy of Sciences, Qingdao 266071, China; [3]National High Magnetic Field Laboratory and Department of Earth, Ocean and Atmospheric Science, Florida State University, Tallahassee, FL 32306, USA; [4]Department of Marine Geology and Geophysics, Woods Hole Oceanographic Institution, Woods Hole, MA 02543, USA

*Corresponding author. Telephone: 86 13816928099. E-mail: zhouhy@tongji.edu.cn
†Present address: American Chemical Society, 1155 Sixteenth Street, N.W., Washington, DC 20036, USA.

Received 4 August 2016; Accepted 18 June 2020

ABSTRACT

Mantle source heterogeneity and magmatic processes have been widely studied beneath most parts of the Southwest Indian Ridge (SWIR). But less is known from the newly recovered mid-ocean ridge basalts from the Dragon Bone Amagmatic Segment (53°E, SWIR) and the adjacent magmatically robust Dragon Flag Segment. Fresh basalt glasses from the Dragon Bone Segment are clearly more enriched in isotopic composition than the adjacent Dragon Flag basalts, but the trace element ratios of the Dragon Flag basalts are more extreme compared with average mid-ocean ridge basalts (MORB) than the Dragon Bone basalts. Their geochemical differences can be explained only by source differences rather than by variations in degree of melting of a roughly similar source. The Dragon Flag basalts are influenced by an arc-like mantle component as evidenced by enrichment in fluid-mobile over fluid-immobile elements. However, the sub-ridge mantle at the Dragon Flag Segment is depleted in melt component compared with a normal MORB source owing to previous melting in the subarc. This fluid-metasomatized, subarc depleted mantle is entrained beneath the Dragon Flag Segment. In comparison, for the Dragon Bone axial basalts, their Pb isotopic compositions and their slight enrichment in Ba, Nb, Ta, K, La, Sr and Zr and depletion in Pb and Ti concentrations show resemblance to the Ejeda–Bekily dikes of Madagascar. Also, Dragon Bone Sr and Nd isotopic compositions together with the Ce/Pb, La/Nb and La/Th ratios can be modeled by mixing the most isotopically depleted Dragon Flag basalts with a composition within the range of the Ejeda–Bekily dikes. It is therefore proposed that the Dragon Bone axial basalts, similar to the Ejeda–Bekily dikes, are sourced from subcontinental lithospheric Archean mantle beneath Gondwana, pulled from beneath the Madagascar Plateau. The recycling of the residual subarc mantle and the subcontinental lithospheric mantle could be related to either the breakup of Gondwana or the formation and accretion of Neoproterozoic island arc terranes during the collapse of the Mozambique Ocean, and is now present beneath the ridge.

Key words: Southwest Indian Ridge; mid-ocean ridge basalts; incompatible elements; isotopes

INTRODUCTION

Understanding variations in mantle sources and magmatic processes through geochemistry of mid-ocean ridge basalts is critical to determining the dynamics and compositional evolution of the upper mantle (e.g. Langmuir *et al.*, 1992; Ito & Mahoney, 2005; Sun, 2016). The Southwest Indian Ridge, spreading at 14–16 mm a^{-1} (DeMets *et al.*, 2010), as an iconic ultraslow ridge (Dick *et al.*, 2003) with variable melt production and discontinuous crustal thickness can thus act as a unique window to investigate upper mantle heterogeneity (e.g. Nauret *et al.*, 2011). With its extreme obliquity to the spreading direction, mantle upwelling is slowed to the point where melting is highly attenuated owing to conductive heat loss and the formation of a thicker lithospheric lid (e.g. Reid & Jackson, 1981; Bown & White, 1994). As a result, overall, magma production is highly sensitive to mantle source composition, and the crust is thin, highly variable in thickness, and often missing (Zhou & Dick, 2013). Magmatic and amagmatic modes of spreading alternate ubiquitously along the ridge (e.g. Dick *et al.*, 2003; Cannat *et al.*, 2006, 2008, Sauter *et al.*, 2013), probably reflecting large along-axis variations in ridge geometry and mantle source. The ridge axis between 48 and 53°E provides a conspicuous example of the variability encountered along the SWIR, reflecting extreme variations in crustal thickness that reflect large changes in the tectonic setting and composition of the mantle source over a few hundred kilometers (Zhao *et al.*, 2013; Zhou & Dick, 2013; Li *et al.*, 2015; Gao *et al.*, 2016; Yang *et al.*, 2017).

The 48–53°E section of the Southwest Indian Ridge consists of two strongly contrasting ridge segments: the magmatically robust 350 km long eastern section (48°25′–52°18′E) of the 600 km long Dragon Flag Supersegment (46°12′–52°18′E) and the 80 km Dragon Bone Amagmatic Segment (52°22′–53°21′E). These are separated by the 110 km offset Gallieni Fracture Zone at 52°20′E, one of the deepest and largest transforms on the SWIR (Sauter *et al.*, 2001, 2009). The Dragon Flag Supersegment is named here for the well-known Dragon Flag hydrothermal area, which lies at 49°39′E (Tao *et al.*, 2012; Zhao *et al.*, 2013). Sampling along the eastern Dragon Flag Supersegment has recovered numerous depleted mid-ocean ridge basalt (D-MORB) glasses (Gale *et al.*, 2013) along its central portion. Seismic studies show crust between 3 and 10 km thick (Sauter *et al.*, 2001; Zhao *et al.*, 2013; Li *et al.*, 2015; Niu *et al.*, 2015), possibly some of the thickest crust anywhere along the SWIR. The adjacent Dragon Bone Segment, east of the Gallieni Fracture Zone, in turn reflects the lack of significant crust and hydrothermal area compared with its sister segment to the west. Only scattered basalt and vast areas of mantle are exposed on the seafloor immediately east of the Gallieni Fracture Zone. In contrast to the Dragon Flag Segment D-MORB, high-sodium enriched MORB (E-MORB) glasses were sampled along the Dragon Bone Segment axis, with transitional MORB found only in the rift mountains 70 km to the south. These basalts located on the two adjacent segments but with remarkably different geochemical characteristics are therefore of inherent interest.

Although numerous geophysical and geological studies of the two segments adjacent to Gallieni Transform have been conducted (Sauter *et al.*, 2001; Zhao *et al.*, 2013; Zhou & Dick, 2013; Chen *et al.*, 2015; Li *et al.*, 2015, 2017; Niu *et al.*, 2015; Gao *et al.*, 2016; Yang *et al.*, 2017; Wang *et al.*, 2019), few studies have considered the differences in geochemistry between the two segments, and none have investigated the Dragon Bone basalts.

Several possible origins for MORB from the central SWIR have been proposed previously. For example, E-MORB between 36 and 39°E were suggested to be influenced by Marion and Prince Edward Island lavas (Janney *et al.*, 2005). For basalts from 39 to 41°E, an involvement of subcontinental lithospheric mantle (SCLM) was invoked for their source (Mahoney *et al.*, 1992; Janney *et al.*, 2005), whereas Meyzen *et al.* (2005) argued for the presence of lower continental crust in their source mantle. For the isotopically enriched normal (N)-MORB at 50·5°E, Yang *et al.* (2017) argued for the influence of the Crozet hotspot, which is 900 km away from the SWIR.

We here report new major and trace element and Sr–Nd–Pb isotopic data for the high-sodium E-MORB from the Dragon Bone axis as well as the depleted MORB from the Dragon Flag Segment. Using these data we re-evaluate the source origins for the Dragon Flag basalts and determine whether the geochemical differences between the Dragon Bone and Dragon Flag Segment basalts are related to source heterogeneity or post-melting differences in sampling similar sources.

GEOLOGICAL SETTING AND SAMPLE LOCATIONS

The study area is located between the Indomed (46°E) and Gazelle (54°06′E) fracture zones, and is separated by the Gallieni Fracture Zone (52°20′E) into two morphologically distinct regions. The eastern portion of the Dragon Flag Supersegment trends 74° oblique to the spreading direction, and consists of six en echelon short magmatic segments separated by non-transform discontinuities. The eastern 80 km Dragon Bone Segment extends from the Gallieni to the 80 km offset Gazelle Fracture Zone (Fig. 1a). Multi-beam bathymetry from the RV *Dayang Yihao* cruises shows that the eastern Dragon Flag rift valley is ~1000 m shallower on average than the Dragon Bone rift valley (3090 m vs 4000 m depth).

Following the segmentation assigned by Cannat *et al.* (1999) our basalts come from Dragon Flag segments 30, 29, 28, and 27, and Dragon Bone segment 24 (Fig. 1b). The shallowest segment (27) shoals to

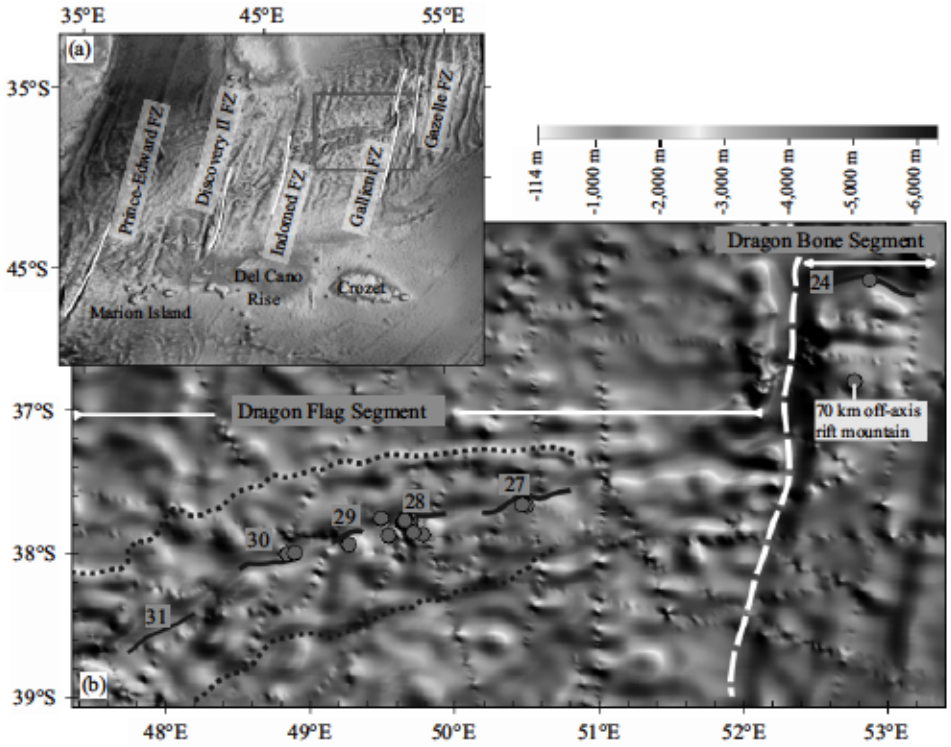

Fig. 1. (a) Bathymetric map of the central Southwest Indian Ridge, with large fracture zones (FZ) and highlands labeled Marion Island, Del Cano Rise and Crozet. The red rectangle is shown enlarged in (b). (b) Dragon Flag Segment and the Dragon Bone Amagmatic Segment with sample locations. Fine dotted lines outline the anomalous elevated terrain flanking the Dragon Flag Supersegment (Sauter *et al.*, 2001, 2009). Dashed line marks the Gallieni Fracture Zone. Bold black lines show discrete segments offset by non-transform discontinuities.

<1500 m and is ~60 km long with high along-axis relief and a large mantle Bouguer anomaly (MBA) low (Sauter *et al.*, 2001; Li *et al.*, 2015). Its crustal thickness has been seismically measured, reaching 10·2 km near its midpoint, before tapering down at the segment ends (Li *et al.*, 2015; Niu *et al.*, 2015).

Segment 28 is an ~30 km long narrow segment with an ~5 km wide neovolcanic ridge at its center. A deep basin with the Dragon Flag Oceanic Core Complex and associated hydrothermal area marks the axial discontinuity between segments 28 and 27. Shoaling to only 3000 m, with much smaller along-axis relief, and smaller MBA low, segment 28 is magmatically less robust with a crustal thickness of only 5–6 km (Sauter *et al.*, 2004, 2009; Zhao *et al.*, 2013). The overall crustal thickness beneath the segment center is greater than that beneath the southern ridge flank (~3·0–4·0 km) (Sauter *et al.*, 2009; Zhao *et al.*, 2013), probably reflecting asymmetric spreading accompanying core complex formation.

Segments 29 and 30 are similar to segment 28. Segment 29 is the smallest, and is bounded by deeper and larger non-transform discontinuities, indicating weak present-day magmatism. Segment 30 is shallower than segment 29 and is ~40 km long, indicating more robust magmatism.

Segment 24 to the east of the Gallieni Fracture Zone is much deeper than any of the segments to the west. It has an unusual morphology, being bowed to the north, with 2400 m along-axis relief shoaling to 3900 m at its midpoint. The deep bathymetry and large exposure of peridotites indicate cold mantle and weak magmatism (Zhou & Dick, 2013). Coordinates and tectonic setting of each sampling location are reported in Table 1.

PETROGRAPHY

Most of the basalts analyzed are from quenched pillow basalt glass rinds, whose thickness ranges from very thin (<5 mm thick; e.g. Supplementary Fig. S1a, b, h and i; supplementary data are available for downloading at http://www.petrology.oxfordjournals.org) to relatively thick (>2 cm thick; e.g. Supplementary Fig. S1b and c). Several samples are in the form of small glass marbles (e.g. Supplementary Fig. S1d and e; diameter ~2 cm) and one fist-sized of chunk of glass with a hydrated fracture network (Supplementary Fig. S1g). The basalts vary considerably in phenocryst content, ranging from pure glass (e.g. Supplementary Fig. S1b and d) to microphenocryst rich. Generally, the microphenocryst population increases from the glassy rim

Table 1: Coordinates and tectonic settings of each sampling station

Station	Longitude (°E)	Latitude (°S)	Depth (mbsl)	No. of samples	Tectonic setting
Dragon Flag Segment					
Segment 30					
34-II-TVG1	48·8418	37·9991	2301	2	neo-volcanic zone
34-II-TVG2	48·8942	37·9967	3006	2	neo-volcanic zone
Segment 29					
34-II-TVG24	49·2662	37·9376	1630	1	southern axial valley wall
30-IV-D8	49·5406	37·8740	2813	2	southern basin wall
30-IV-D9	49·4875	37·7535	3043	1	northern basin wall
Segment 28					
21-V-D13	49·6507	37·7825	2748	1	base of southern wall of axial valley
21-V-TVG1	49·6480	37·7828	2784	1	base of southern wall of axial valley
30-II-TVG10	49·6385	37·7819	2936	2	base of southern wall of axial valley
30-IV-D7	49·6448	37·7901	2798	2	base of southern wall of axial valley
30-IV-D10	49·6553	37·7860	2576	1	base of southern wall of axial valley
30-IV-TVG2	49·6503	37·7832	2805	2	base of southern wall of axial valley
30-IV-TVG4	49·6882	37·7385	2945	1	base of southern wall of axial valley
34-I-TVG4	49·7027	37·7687	3090	2	southern wall of axial valley
34-II-TVG13	49·6901	37·7819	2243	2	southern wall of axial valley
34-II-TVG14	49·6613	37·7643	3153	2	base of southern wall of axial valley
34-IV-TVG4	49·6689	37·7834	2806	2	southern wall of axial valley
34-IV-TVG5	49·6529	37·7696	2974	2	base of southern wall of axial valley
30-II-TVG3	49·7819	37·8643	1540	1	southern ridge flank, 10 km off-axis
30-IV-D12	49·7125	37·8512	1742	2	southern ridge flank, 12 km off-axis
Segment 27					
30-IV-D13	50·4808	37·6585	1802	1	axial center
34-III-TVG1	50·4961	37·6624	1840	2	axial center
34-III-TVG5	50·4661	37·6564	1702	2	axial center
Segment 24-Dragon Bone axis					
30-IV-D2	52·8752	36·1063	3577	3	axial center
Dragon Bone rift mountain					
21-V-D2	52·7672	36·8034	1789	1	southern rift mountain, 70 km off-axis

Sample numbers in the text are in the form 'Cruise #-Leg #-Type-Station #-Sample #'. Sampling type is either a dredge (D) or a TV grab (TVG).

towards the more crystalline interior of the pillow. Slightly cryptocrystalline areas have olivine microphenocrysts, phenocrysts, and crystallites surrounded by dark rims (e.g. Supplementary Fig. S1e and f). Several samples are relatively rich in small plagioclase microphenocrysts, which tend to increase in abundance towards the interior of the original pillow basalt (e.g. Supplementary Fig. S1a). Euhedral to subhedral primitive olivine phenocrysts ($Fo_{90.2–91.6}$) were found in two samples (e.g. Supplementary Fig. S1c and e). Basalt glass DY21-V-D2 from the rift mountains of the Dragon Bone Segment is the only one of our basalts containing coarse plagioclase phenocrysts (Supplementary Fig. S1h), although plagioclase phenocrysts (An_{81}) also occur in the DY30-IV-D2 basalts from the segment center.

ANALYTICAL METHODS

Thirty-six glass samples from seven dredges and 15 TV-grabs from the west segments 27–30 and four glass samples from two dredges from the east Dragon Bone Segment were analyzed. Samples were polished to 100 μm thick thin sections, and were studied with an optical microscope. Major element contents (Table 2) were determined *in situ* by JEOL JAX-8100 electron microprobe at Analytical Laboratory of Beijing Research Institute of Uranium Geology (Reed, 2005) using 2 μm beam diameter at 20 kV acceleration voltage and 1×10^{-8} A. For standardization SPI international standards was used and relative errors for TiO_2 and Na_2O are less than 5%, for SiO_2, Al_2O_3, FeO, MgO and CaO less than 2%, and for MnO, P_2O_5 and K_2O less than 10%.

Trace elements were determined for 18 basalts by laser ablation inductively coupled plasma mass spectrometry (LA-ICP-MS). Glass fragments were crushed and pure fresh glasses were hand-picked under a binocular microscope and mounted using epoxy in holes in an Al-disk. Sample surfaces were highly polished, and samples were analyzed using an Electro Scientific Instruments (ESI) New Wave UP193 FX excimer (193 nm) LA system coupled to a Thermo Element XR ICP-MS system housed at the Geochemistry Program of the National High Magnetic Field Laboratory, Florida State University. Laser energy flux of 6–8 J cm^{-2} was used. Analysis was carried out on 100 μm spots at 50 Hz repetition rate and 20 s dwell time, with USGS basalt standards: BCR-2g, BHVO-2g, and BIR-1g, and NIST SRM 610 (Jochum *et al.*, 2011; Yang *et al.*, 2015). Sample reproducibility is generally better than 2%. Five spots were analyzed for each sample and the averages are reported in Table 3.

Seventeen basalts were also analyzed for Sr–Nd–Pb isotopes on 90–110 mg of handpicked glass. Leaching, dissolution, column chemistry and measurements were

Table 2: Major element compositions of Dragon Flag and Dragon Bone basalts (wt%)

Sample	SiO_2	TiO_2	Al_2O_3	FeO^t	MnO	MgO	CaO	Na_2O	K_2O	P_2O_5	Total
Dragon Flag type 1 basalts											
Segment 28											
30-IV-TVG04-2	49·54	0·66	15·60	7·95	0·16	9·49	13·65	1·85	0·01	0·01	99·20
Segment 27											
34-III-TVG01-1	49·47	1·44	14·83	10·42	0·20	7·12	11·55	2·76	0·08	0·13	98·04
34-III-TVG01-2	49·25	1·47	14·51	10·26	0·19	7·15	11·50	2·92	0·06	0·15	97·52
34-III-TVG05-1	49·79	0·88	16·92	8·91	0·15	8·86	11·33	2·87	0·05	0·06	99·87
34-III-TVG05-2	47·81	0·80	17·68	8·82	0·15	8·84	11·60	2·54	0·03	0·05	98·38
30-IV-D13-1	48·10	0·78	17·58	8·48	0·15	8·86	11·53	2·72	0·05	0·02	98·42
Dragon Flag type 2 basalts											
Segment 30											
34-II-TVG01-3	49·68	1·61	14·93	10·87	0·20	8·08	10·76	2·52	0·08	0·17	99·02
34-II-TVG01-4	48·98	1·50	14·85	10·33	0·24	8·17	10·72	2·56	0·06	0·16	97·59
34-II-TVG01-4 (d)	49·16	1·61	14·89	10·46	0·20	8·18	10·76	2·65	0·07	0·12	98·14
34-II-TVG02-4	49·72	1·34	14·84	10·29	0·19	7·35	11·47	2·56	0·05	0·13	97·97
34-II-TVG02-6	50·09	1·37	14·92	10·39	0·18	7·39	11·67	2·47	0·05	0·13	98·69
Segment 29											
34-II-TVG24-3	48·98	1·58	14·86	10·75	0·21	7·70	10·70	2·71	0·05	0·15	97·75
Segment 28											
30-IV-D09-1	49·76	1·64	14·46	10·51	0·18	7·63	10·45	2·81	0·08	0·15	97·76
30-IV-D08-1	49·34	1·11	15·85	9·38	0·18	8·94	10·98	2·57	0·06	0·12	98·58
30-IV-D08-2	48·89	1·22	15·62	9·41	0·15	9·02	11·15	2·51	0·03	0·07	98·10
30-II-TVG10-1	49·21	1·31	15·07	9·29	0·14	8·44	11·17	2·63	0·05	0·10	97·72
30-II-TVG10-2	49·93	1·31	15·02	9·10	0·16	8·54	11·14	2·74	0·05	0·12	98·39
30-IV-D07-1	48·73	1·19	15·88	9·47	0·16	8·87	10·98	2·56	0·04	0·11	98·09
30-IV-D07-2	48·69	1·14	15·81	9·39	0·19	9·03	11·15	2·51	0·05	0·08	98·14
21-V-TVG01-4	49·25	1·40	14·84	9·68	0·19	8·62	10·82	2·48	0·06	0·12	97·53
30-IV-TVG02-7	49·50	1·40	14·95	9·11	0·19	8·43	10·86	2·65	0·09	0·16	97·63
30-IV-TVG02-6	49·65	1·35	14·95	9·34	0·16	8·46	10·68	2·73	0·09	0·14	97·85
21-V-D13-4	48·94	1·28	15·09	9·49	0·21	8·21	11·17	2·58	0·05	0·15	97·22
34-IV-TVG05-3	49·27	1·43	15·02	9·75	0·17	8·51	10·83	2·49	0·06	0·15	97·73
34-IV-TVG05-1	49·14	1·45	15·02	9·71	0·18	8·75	10·81	2·69	0·05	0·11	97·95
30-IV-D10-12	50·22	1·57	15·06	9·71	0·18	7·07	10·85	2·90	0·09	0·13	97·81
34-II-TVG14-2	49·74	1·39	15·44	9·82	0·19	7·67	11·10	2·30	0·06	0·11	97·90
34-II-TVG14-1	49·11	1·41	15·27	9·72	0·17	7·85	11·09	2·58	0·04	0·11	97·42
34-IV-TVG04-2	49·17	1·56	14·61	10·46	0·20	7·10	11·30	2·73	0·07	0·12	97·34
34-IV-TVG04-3	49·46	1·46	14·89	10·36	0·22	7·08	11·28	2·78	0·08	0·14	97·77
34-II-TVG13-2	49·59	1·15	15·45	9·52	0·20	8·24	12·41	2·04	0·02	0·09	98·77
34-II-TVG13-5	48·99	1·15	15·22	9·07	0·21	8·32	12·50	2·31	0·02	0·08	97·93
34-I-TVG04-40	49·61	1·32	15·47	9·39	0·14	8·13	11·29	2·41	0·08	0·16	98·09
34-I-TVG04-41	49·19	1·39	15·46	9·48	0·19	7·99	11·40	2·62	0·04	0·08	97·94
Segment 28											
30-IV-D12-5	49·79	1·30	15·09	9·48	0·19	8·11	10·86	2·70	0·07	0·04	97·67
30-IV-D12-7	49·81	1·34	14·81	9·85	0·18	8·19	10·74	2·65	0·06	0·10	97·76
30-II-TVG03-3	49·82	1·55	14·79	10·41	0·22	7·29	10·91	2·71	0·08	0·11	98·19
Dragon Bone axial basalts											
30-IV-D2-1	51·87	1·69	16·44	8·33	0·19	6·38	9·44	4·22	0·28	0·13	98·99
30-IV-D2-2	50·72	1·75	16·43	8·71	0·20	5·93	9·56	4·46	0·28	0·27	98·37
30-IV-D2-3	50·84	1·53	16·56	8·55	0·16	6·28	9·40	4·22	0·29	0·22	98·15
Dragon Bone rift mountain											
21-V-D2	48·86	1·34	16·38	9·10	0·18	7·86	10·87	3·02	0·09	0·12	98·09
Parental melts											
Dragon Flag type 2*	49·13	1·01	17·42	7·99	0·18	9·47	11·29	2·50	0·06	0·10	100·00
Dragon Bone axis†	50·69	1·06	17·95	6·30	0·14	9·13	10·08	3·61	0·18	0·13	99·99

FeO^t is total Fe. (d), duplicate.
*Fe_2O_3 content of the parental melt of the Dragon Flag type 2 basalts is 0·85 wt%.
†Fe_2O_3 content of parental melt of the the Dragon Bone axial basalts is 0·72 wt%.

carried out at the National High Magnetic Field Laboratory, Florida State University using methods described by Mallick *et al.* (2014). The separates were leached in ~5 ml 2·5N HCl and ~500 µl <30% H_2O_2 for 20–30 min at room temperature to remove any alteration products. The leached separates were rinsed several times with quartz sub-boiling distilled water. Subsequent dissolution and column chemistry was performed after procedures described by Stracke *et al.* (2003). Sr isotope compositions were measured by thermal ionization mass spectrometry (TIMS) using a Finnigan MAT 262 RPQ system. Measured value of the Eimer & Amend (E&A) $SrCO_3$ standard is $^{87}Sr/^{86}Sr = 0·708000 \pm 0·000007$ (2σ, $n=6$). The $^{87}Sr/^{86}Sr$ ratios are corrected for mass bias using $^{88}Sr/^{86}Sr = 0·1194$ and reported to the E&A $SrCO_3$ standard of $^{87}Sr/^{86}Sr = 0·708000$. Blanks for Sr were <100 pg. Nd and Pb isotopes were measured using a Neptune multi-

Table 3: Trace element compositions of basalts from the Dragon Flag and Dragon Bone segments (ppm)

	Dragon Flag type 1 basalts				Dragon Flag type 2 basalts						
	30IV-TVG04-2	34III-TVG01-1	34III-TVG05-1	30IV-D13-1	30-IV-D09-1	30-IV-D08-1	30-IV-D08-2	30-II-TVG10-1	30-IV-D07-1	30-IV-D07-2	30-IV-TVG02-6
Sc	35	42	32	31	39	35	36	37	34	36	38
Rb	0·19	1·12	0·34	0·55	1·01	0·44	0·39	0·61	0·37	0·55	1·03
Sr	42·43	113	127	127	92	87	88	89	89	87	98
Y	16·65	29·77	16·27	15·81	43·32	26·36	26·97	35·66	30·54	26·46	33·28
Zr	18·87	77	43	41	102	56	57	79	62	56	85
Nb	0·20	1·32	0·52	0·52	1·69	0·65	0·66	1·05	0·75	0·73	1·27
Cs	0·89	0·21	0·08	0·18	0·02	0·06	0·02	0·02	0·01	0·24	0·11
Ba	2·11	7·81	2·24	2·13	10·2	3·41	3·48	5·35	3·61	3·56	7·04
La	0·46	2·37	1·30	1·34	2·99	1·43	1·47	2·12	1·66	1·46	2·41
Ce	1·72	8·11	4·58	4·37	9	5·21	5·3	6·76	5·3	5·3	8·31
Pr	0·36	1·40	0·78	0·74	1·69	0·98	1·01	1·29	1·01	1·01	1·54
Nd	2·38	7·87	4·26	4·10	10·85	5·89	5·97	8·39	6·59	5·96	8·82
Sm	1·23	3·00	1·54	1·47	4·11	2·43	2·47	3·29	2·64	2·45	3·39
Eu	0·54	1·17	0·71	0·67	1·44	0·98	1·01	1·19	1·03	1·00	1·24
Gd	1·97	3·90	2·03	1·99	5·11	3·46	3·53	4·14	3·39	3·48	4·64
Tb	0·41	0·74	0·39	0·37	1·07	0·66	0·69	0·86	0·72	0·68	0·88
Dy	2·99	5·07	2·62	2·57	7·42	4·72	4·9	6·06	5·2	4·82	6·07
Ho	0·66	1·11	0·57	0·55	1·59	1·03	1·07	1·3	1·12	1·05	1·32
Er	1·99	3·22	1·70	1·63	4·76	3·07	3·21	3·9	3·39	3·14	3·89
Tm	0·29	0·47	0·24	0·23	0·69	0·44	0·45	0·56	0·49	0·46	0·55
Yb	1·99	3·09	1·61	1·61	4·49	3·03	3·14	3·7	3·23	3·08	3·79
Lu	0·29	0·47	0·24	0·24	0·68	0·44	0·46	0·55	0·49	0·44	0·55
Hf	0·73	2·11	1·01	0·98	2·96	1·64	1·74	2·34	1·82	1·68	2·48
Ta	0·01	0·08	0·03	0·04	0·1	0·04	0·04	0·06	0·05	0·04	0·08
Pb	0·95	2·65	1·19	1·85	1·01	0·71	0·52	0·85	0·57	0·75	0·94
Th ppb	18	132	44	47	136	51	51	86	58	52	116
U ppb	7	60	15	16	44	26	22	28	22	25	42

	Dragon Flag type 2 basalts			Dragon Bone axial basalts			Dragon Bone rift mountain	Standards			
	30-IV-TVG02-7	30-IV-D12-5	30-IV-D12-7	30-IV-D2-1	30-IV-D2-2	30-IV-D2-3	21-V-D2	NIST 610	BCR-2g	BIR-1g	BHVO-2g
Sc	38	38	38	32	32	33	37	441	33	43	33
Rb	1·03	0·84	0·83	3·07	3·17	3·19	1·01	425·7	47	0·197	9·2
Sr	96	88	86	201	202	197	136	515·5	342	109	396
Y	32·5	31·94	30·92	38·86	39·47	34·36	28·3	450	35		26
Zr	83	73	71	166	166	146	86	440	184	14	170
Nb	1·25	1·13	1·14	6	6·11	5·32	1·86	419	12·5	0·52	18·3
Cs	0·11	0·05	0·04	0·04	0·05	0·08	0·08	361	1·16	0·007	0·1
Ba	6·86	7·83	7·75	44·8	45·3	43·2	11·1	435	683	6·5	131
La	2·34	2·1	2·06	7·59	7·65	6·77	3·1	457	24·7	0·609	15·2
Ce	8·07	6·97	7·23	18·2	19·13	18·52	9·78	448	53·3	1·89	37·6
Pr	1·49	1·3	1·32	2·86	2·88	2·88	1·65	430	6·7	0·37	5·35
Nd	8·53	7·65	7·59	15·68	15·76	14·31	8·87	431	28·9	2·37	24·5
Sm	3·3	3·08	2·96	4·66	4·68	4·36	3·07	451	6·59	1·09	6·1
Eu	1·21	1·17	1·14	1·59	1·60	1·56	1·18	461	1·97	0·517	2·07
Gd	4·54	4·28	4·16	5·27	5·25	5·42	4·07	444	6·71	1·85	6·16
Tb	0·85	0·82	0·8	0·99	0·99	0·94	0·75	443	1·02	0·35	0·92
Dy	5·99	5·8	5·58	6·77	6·75	6·33	5·21	427	6·44	2·55	5·28
Ho	1·28	1·26	1·2	1·44	1·42	1·34	1·11	449	1·27	0·56	0·98
Er	3·8	3·74	3·6	4·24	4·23	3·97	3·31	426	3·7	1·7	2·56
Tm	0·54	0·53	0·5	0·61	0·61	0·55	0·48	420	0·51	0·24	0·34
Yb	3·71	3·69	3·51	4·01	4	3·88	3·28	445	3·39	1·64	2·01
Lu	0·54	0·53	0·51	0·61	0·6	0·56	0·48	435	0·503	0·248	0·279
Hf	2·43	2·2	2·12	3·55	3·51	3·27	2·34	432	4·84	0·57	4·32
Ta	0·08	0·08	0·07	0·36	0·35	0·32	0·13	452	0·78	0·036	1·15
Pb	1·07	0·85	0·93	1·49	1·35	1·57	0·85	426	11	3·7	1·7
Th ppb	111	106	97	497	489	442	130	457·2	5·9	0·03	1·22
U ppb	51	35	45	130	130	137	44	461·5	1·69	0·023	0·403

collector (MC-)ICP-MS system (Mallick *et al.*, 2014). The estimated uncertainties are based on repeated measurements of the standards. The measured value of the La Jolla standard is $^{143}Nd/^{144}Nd = 0{\cdot}511794 \pm 0{\cdot}000004$ (2σ, $n = 5$). The $^{143}Nd/^{144}Nd$ ratios are corrected for mass bias using a $^{146}Nd/^{144}Nd$ ratio of 0·7219 and are reported relative to La Jolla standard of 0·511850. Blanks for Nd were ~10 pg. Pb standard NBS 981

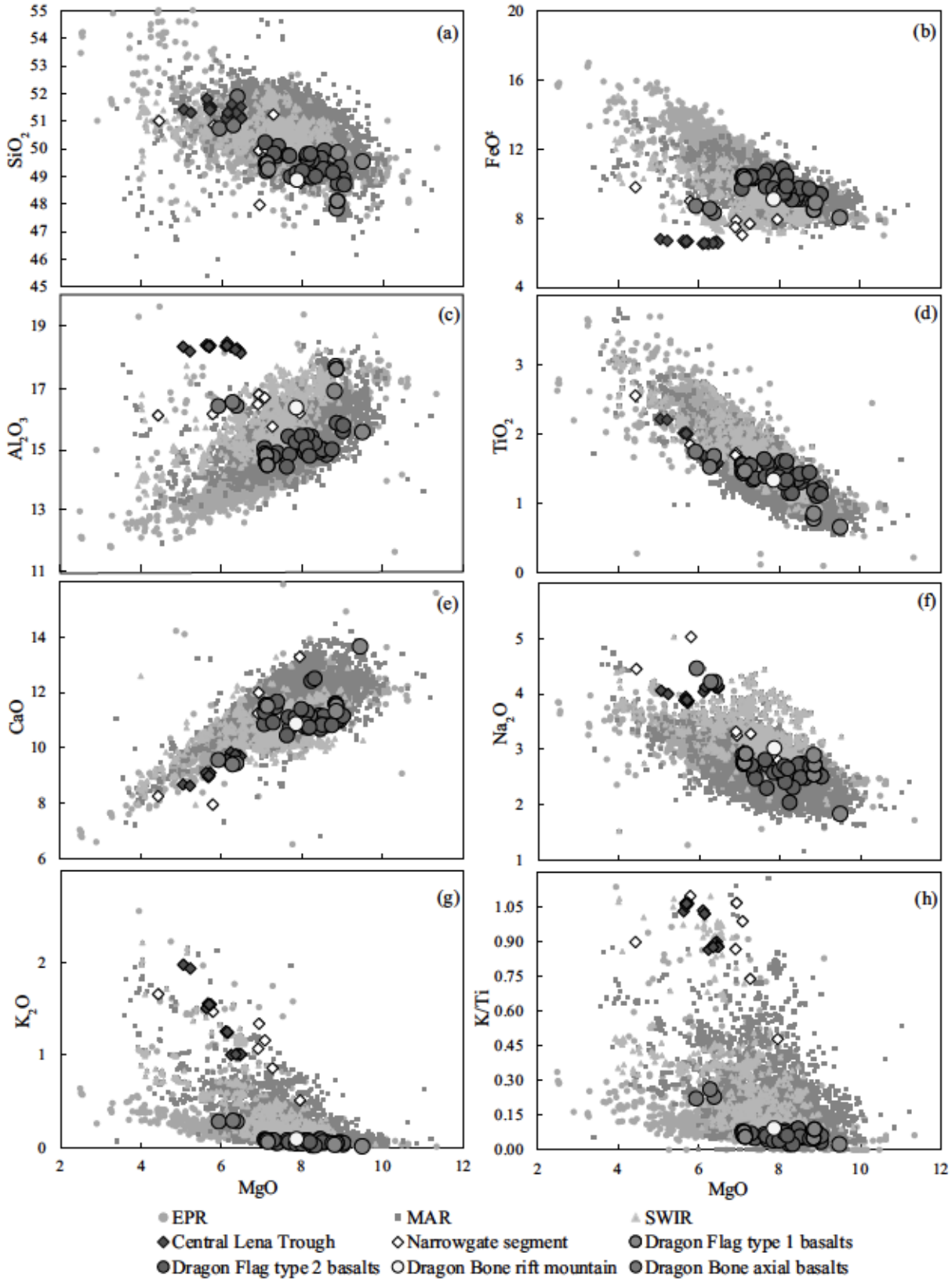

Fig. 2. Plots of (a) SiO_2, (b) FeO^t, (c) Al_2O_3, (d) TiO_2, (e) CaO, (f) Na_2O, (g) K_2O and (h) K/Ti vs MgO of basaltic glasses from our study area as well as East Pacific Rise (EPR), Mid-Atlantic Ridge (MAR) and SWIR data from the http://www.earthchem.org/petdb. Central Lena Trough (Nauret *et al.*, 2011) and Narrowgate segment (Standish *et al.*, 2008) data are also compared as they are from the ultra-slow-spreading ridges and with equivalent sodium contents. The Dragon Flag basalts are classified into two groups according to their distinct trace element patterns.

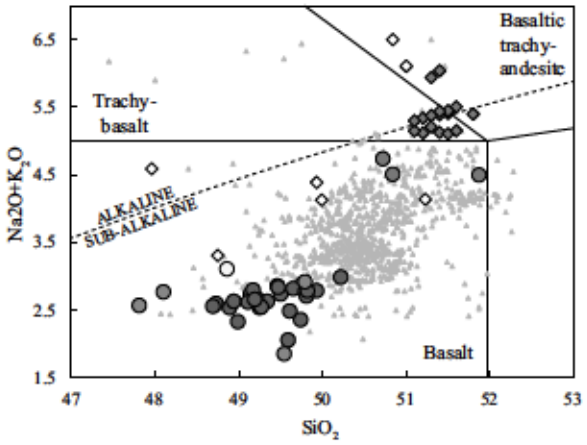

Fig. 3. Total alkalis vs SiO_2 diagram (Middlemost, 1994) showing comparison of the Dragon Bone and Dragon Flag basalts with those from Central Lena Trough, Narrowgate segment and SWIR. Symbols as in Fig. 2.

yielded average values of $^{206}Pb/^{204}Pb = 16{\cdot}929 \pm 0{\cdot}001$ (2σ, $n = 5$), $^{207}Pb/^{204}Pb = 15{\cdot}481 \pm 0{\cdot}001$ (2σ, $n = 5$) and $^{208}Pb/^{204}Pb = 36{\cdot}664 \pm 0{\cdot}003$ (2σ, $n = 5$). Pb-isotopic compositions are corrected for mass bias using a $^{205}Tl/^{203}Tl$ ratio of 2·3889 and are reported relative to NBS 981 standard isotope ratios of $^{206}Pb/^{204}Pb = 16{\cdot}9356$, $^{207}Pb/^{204}Pb = 15{\cdot}4891$ and $^{208}Pb/^{204}Pb = 36{\cdot}7006$ from Todt *et al.* (1996). Blanks for Pb were ~50 pg.

RESULTS

Major element compositions

The Dragon Bone and Dragon Flag basalts show trends of decreasing MgO with increasing SiO_2, FeO, TiO_2 and Na_2O, and decreasing Al_2O_3 and CaO (Fig. 2, Table 2). Dragon Flag basalts analyzed here represent 200 km and four discrete segments of the 350 km long Dragon Flag Supersegment. Although there are significant variations in geomorphology and magmatic activity, their major element compositions show only a limited range. The Dragon Bone rift mountain basalt, except for its higher Al_2O_3 contents, is similar to the Dragon Flag ridge basalts. The Dragon Bone axial basalts appear more fractionated and plot separately from the Dragon Flag samples.

Based on La/Sm and K_2O/TiO_2 ratios Dragon Bone axial basalts show enriched characteristics compared with the average MORB of Gale *et al.* (2013) whereas the Dragon Flag basalts are on average more depleted than average MORB. The Dragon Bone axial basalts are at the high end of the spectrum of global MORB compositions for Al_2O_3, Na_2O and SiO_2, and at the low end for low TiO_2, FeO and CaO (Fig. 2).

The total alkalis diagram (Fig. 3) shows that Dragon Bone axial basalts have uniformly higher alkali contents than the Dragon Flag basalts and the Dragon Bone rift mountain basalt. The Dragon Bone axial basalts are similar in Na_2O content to the high-alkali basalt suite from the Narrowgate segment (Standish *et al.*, 2008) and Central Lena Trough basalts (Nauret *et al.*, 2011). The Dragon Flag and Dragon Bone rift mountain lavas are in the low-silica and low-alkali range for SWIR basalts (data from http://www.earthchem.org/petdb), whereas the Dragon Bone axis basalts plot at the high-silica and high-alkali end (Fig. 3).

Trace element compositions

The Dragon Bone and Dragon Flag basalts display distinguishable ranges of trace element concentrations (Table 3) and ratios that suggest the influence of variable degrees of partial melting of variably depleted and enriched mantle sources. These trace element compositions were obtained as *in situ* measurements on fresh basaltic glass and thus are not affected by seawater alteration processes.

Dragon Flag basalts

The Dragon Flag basalts show limited variations in trace element concentrations and range from similar to the average D-MORB to more depleted than it (Gale *et al.*, 2013). Three samples (30IV-D13-1 and 34III-TVG5-1 from segment 27 and 30IV-TVG4-2 from segment 28) are the most depleted ever found in the global MORB data at relatively primitive MgO contents. One sample, 34III-TVG1-1 from segment 27, with lower MgO (7·2 wt%), has higher trace elements concentrations owing to fractional crystallization. We group these four samples as the Dragon Flag type 1 basalts to distinguish them from the main group of the Dragon Flag basalts (type 2) that plots below the average D-MORB but above the lower bound of global MORB (Gale *et al.*, 2013). The Dragon Flag basalts with $(La/Sm)_{PM} < 0{\cdot}5$ (normalized to primitive mantle; Sun & McDonough, 1989), are at the depleted end of the range for Southwest Indian Ridge MORB. Primitive mantle normalized diagrams of the Dragon Flag basalts and the average D-MORB as well as the lower bound of global MORB are displayed in Fig. 4a and b.

The Dragon Flag type 2 basalts plot within the range of MORB in limited Zr/Hf (33–37) and Nb/Ta (15–18) ranges, whereas the type 1 basalts spread over a much wider range: (1) the most depleted basalt (sample 30IV-TVG4-2) plots at the lower end of the MORB compositional spectrum (Nb/Ta_{MORB} = 11·5–16·6, Zr/Hf_{MORB} = 27·77–43·68; Münker *et al.*, 2003) and one spot analysis of this sample (Nb/Ta = 9·8 and Zr/Hf = 24) is similar to the depleted mantle composition (Münker *et al.*, 2003; Weyer *et al.*, 2003); (2) the other three samples (30IV-D13-1, 34III-TVG1-1 and 34III-TVG5-1 from segment 27) have Nb/Ta and Zr/Hf ratios around 15·5 and within 37–40 respectively, plotting within the ocean island basalt (OIB) field (Nb/Ta_{OIB} = 11·5–16·6, Zr/Hf_{OIB} = 27·77–43·68; Münker *et al.*, 2003). The Dragon Flag type 1 basalts show negative anomalies in immobile elements Nb, Ta

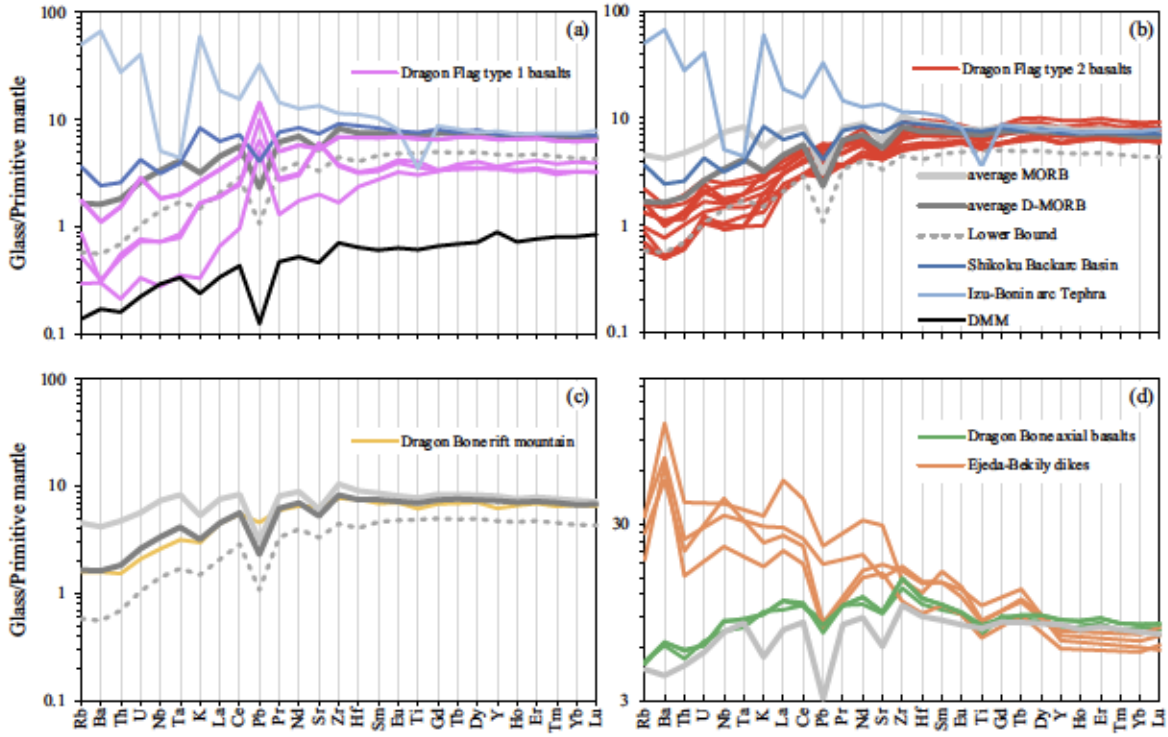

Fig. 4. Primitive mantle normalized trace element patterns. Normalization constants are from Sun & McDonough (1989). (a) Dragon Flag type 1 basalts; (b) Dragon Flag type 2 basalts; (c) the single basalt from the Dragon Bone rift mountain; (d) Dragon Bone axial basalts. Samples in this study are also compared with data of the average MORB and D-MORB compositions, and the lower bound of global MORB data (Gale *et al.*, 2013), basalts from Shikoku backarc basin and Izu–Bonin arc tephra (Straub *et al.*, 2010), a depleted MORB mantle source DMM, (Salters & Stracke (2004) and basalts from the Ejeda–Bekily dikes (Mahoney *et al.*, 1991, 2008).

and Zr and positive anomalies in Ba, Sr and Pb, which are typical characteristics of fluid addition. Thus, we also compare these data with some backarc basin basalts (BABB) and arc basalts (Straub *et al.*, 2009) (Fig. 4a and b). Also, the combinations of fluid-mobile and -immobile elements ratios of the type 1 basalts show an enrichment of fluid-mobile elements (Fig. 5).

Dragon Bone basalts

The Dragon Bone rift mountain basalt is similar to the average D-MORB composition. The Dragon Bone axial basalts are similar to the average MORB composition (Gale *et al.*, 2013) with higher large ion lithosphere elements (LILE) and light rare earth element (REE) concentrations (Fig. 4).

The differences between Dragon Bone axial basalts and Dragon Flag basalts are in both LILE and high field strength elements (HFSE), with the Dragon Bone axial basalts having higher LILE and lower HFSE than the Dragon Flag basalts; for example, Ba and Yb of the Dragon Bone axial basalts vary from 43·2 to 45·5 and from 3·88 to 4·01 respectively, whereas Ba and Yb of the Dragon Flag basalts range from 2·11 to 10·8 and from 1·61 to 4·49 respectively. The high Zr/Hf (~47) ratios of the Dragon Bone axial basalts lie outside the field of MORB (e.g. Münker *et al.*, 2003; Pfänder *et al.*, 2012). Thus, it is clear that the Dragon Bone axial basalts and Dragon Flag basalts are distinct from each other.

Sr–Nd–Pb isotopes compositions

We report new Sr–Nd–Pb isotopes data for the Dragon Flag and Dragon Bone basalts (Table 4). The isotopic compositions of the Dragon Flag basalts are similar to those of other SWIR basalts (Mahoney *et al.*, 1992; Chauvel & Blichert-Toft, 2001; Meyzen *et al.*, 2005, 2007; Yang *et al.*, 2017). Although distributed along the 140 km long segment, the Dragon Flag type 2 basalts are fairly homogeneous, with $^{143}Nd/^{144}Nd$ ranging from 0·513106 to 0·513138, $^{87}Sr/^{86}Sr$ between 0·702722 and 0·703018, and values of $^{206}Pb/^{204}Pb$ of 18·143–18·292, $^{207}Pb/^{204}Pb$ of 15·495–15·479, and $^{208}Pb/^{204}Pb$ of 37·956–38·047. In comparison, the isotopic compositions of the Dragon Flag type 1 basalts show a much wider range with $^{206}Pb/^{204}Pb$ reaching 15·624 (Fig. 6).

The Dragon Bone axial basalts are isotopically more enriched than the Dragon Flag basalts, with lower $^{143}Nd/^{144}Nd$ (0·512997–0·513012) and higher $^{87}Sr/^{86}Sr$ (0·703256–0·703392). The Dragon Bone axial basalts have a wider range in Pb isotopic compositions, with values of $^{206}Pb/^{204}Pb$ of 17·506–18·138, $^{207}Pb/^{204}Pb$ of 15·463–15·549, and $^{208}Pb/^{204}Pb$ of 37·758–38·565. The single rift mountain basalt has similar Sr–Nd–Pb isotopes as the Dragon Flag basalts (Fig. 6).

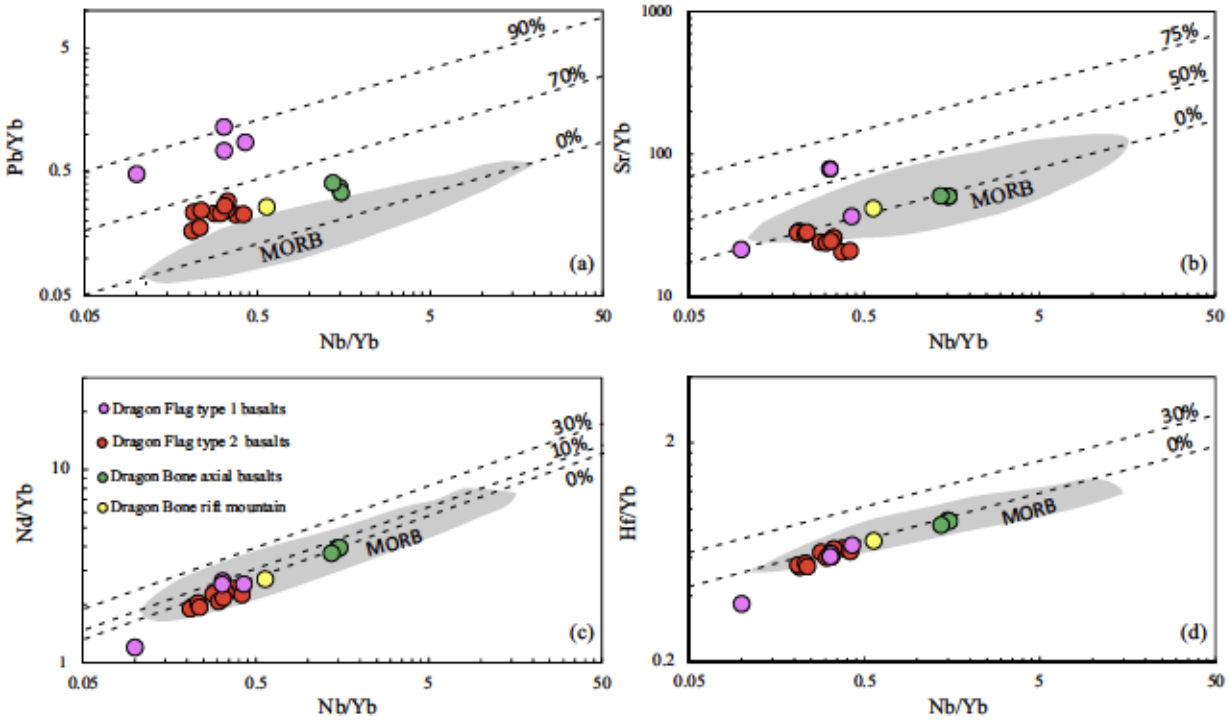

Fig. 5. Fluid-mobile versus fluid-immobile elements ratios of the Dragon Flag type 1 and type 2 basalts, Dragon Bone axial and rift mountain basalts. (a) Pb/Yb, (b) Sr/Yb, (c) Nd/Yb and (d) Hf/Yb vs Nb/Yb. Data are compared with mid-ocean ridge basalts. MORB data are from Niu & Batiza (1997). Dashed lines are estimating percentage of slab-derived Sr, Pb, Nd and Hf. After Pearce *et al.* (1995) and modified from Straub and Zellmer (2012).

DISCUSSION

The trace elements and isotopic compositions show that the Dragon Bone basalts are clearly more enriched in isotopic composition than the adjacent Dragon Flag basalts (Fig. 6), but the trace element ratios of the Dragon Flag basalts are more extreme compared with the average MORB than the Dragon Bone basalts (Fig. 7). These geochemical differences indicate that the Dragon Bone and Dragon Flag basalts probably have different sources. Below we discuss what processes and source compositions are responsible for the Dragon Flag and Dragon Bone basalts variations.

Major element fractionation

The major elements distinguish the Dragon Bone basalts from the Dragon Flag basalts (both type 1 and type 2 basalts) with lower FeO and higher Al_2O_3 and total alkalis at lower MgO contents (Fig. 2), forming separate clusters. The nearly constant CaO/Al_2O_3 and increasing Sc and TiO_2 with decreasing MgO in the Dragon Flag basalts indicate that the Dragon Flag basalts lie on the L + Ol + Pl cotectic, whereas the comparatively lower CaO/Al_2O_3 and Sc at more evolved MgO contents in the Dragon Bone axial basalts would indicate fractional crystallization of Ol + Pl + Cpx. We modeled the liquid lines of descent (LLDs, Supplementary Fig. S2) starting from two different parental melts (Table 2) generated by reverse crystallization of the most evolved basalts from each segment till an Mg# of 72 was reached, as melt with Mg# = 72 is thought to be in equilibrium with a peridotitic mantle (Niu & O'Hara, 2008). The stability field of clinopyroxene expands at the expense of olivine and plagioclase with increasing pressures (e.g. Grove et al., 1992; Lissenberg & Dick, 2008; Standish *et al.*, 2008). The majority of Dragon Flag basalts lie above and along the 1 kbar cotectic (Supplementary Fig. S2), and have not seen clinopyroxene crystallization, suggesting that the Dragon Flag basalts fractionated at low pressures. Increasing the crystallization pressures from the same parental melt as the Dragon Flag basalts cannot explain the Dragon Bone axial basalts and these basalts must have evolved from a different parental melt.

The modeled parental melt of Dragon Flag basalts results in higher MgO and FeO but lower Al_2O_3 and Na_2O contents than that of the Dragon Bone axial basalts. Their parental melts have major element compositions similar to the calculated primary melts at different degrees of melting and pressures after Kinzler (1997). For example, the parental melt of the Dragon Flag basalts is similar to the primary melt from near-fractional aggregated melt by 9% degree of melting at 1·2 GPa and that of the Dragon Bone axial basalts by about 7% degree of melting at 0·95 GPa from a previously depleted primitive upper mantle composition (Hart & Zindler, 1986).

Table 4: Sr–Nd–Pb isotope compositions of basalts from the Dragon Flag and Dragon Bone segments

Sample	$^{87}Sr/^{86}Sr$	±2σ	$^{143}Nd/^{144}Nd$	±2σ	εNd	$^{206}Pb/^{204}Pb$	±2σ	$^{207}Pb/^{204}Pb$	±2σ	$^{208}Pb/^{204}Pb$	±2σ
Dragon Flag type 1 basalts											
30IV-TVG04-2	0·702761	0·000014	0·513114	0·000005	9·4	18·206	0·0032	15·488	0·0029	37·987	0·0068
34III-TVG01-1	0·703039	0·000014				18·624		15·547		38·518	
34III-TVG05-1	0·703172	0·000014	—	—	—	18·227	—	15·487	—	38·030	—
30IV-D13-1	—	—	—	—	—	18·581	—	15·536	—	38·487	—
Dragon Flag type 2 basalts											
30IV-D09-1	0·702942	0·000014	0·513111	0·000008	9·4	18·143	0·0012	15·480	0·0012	37·956	0·0034
30IV-D08-1	0·702723	0·000014	0·513138	0·000006	9·9	18·292	0·0012	15·493	0·0012	38·004	0·0036
30IV-D08-2	0·702767	0·000016	0·513136	0·000008	9·9	18·236	0·0014	15·488	0·0014	37·996	0·0044
30II-TVG10-1	0·702855	0·000014	0·513129	0·000006	9·7	18·186	0·0012	15·487	0·0010	37·978	0·0032
30IV-D07-1	0·702745	0·000014	0·513136	0·000010	9·9	18·234	0·0010	15·486	0·0010	37·985	0·0028
30IV-D07-2	0·702722	0·000014	0·513135	0·000010	9·8	18·242	0·0016	15·486	0·0016	37·990	0·0048
30IV-TVG02-7	0·702935	0·000014	0·513116	0·000008	9·5	18·207	0·0012	15·489	0·0012	38·013	0·0032
30IV-D10-12	0·702962	0·000014	0·513117	0·000014	9·5	18·205	0·0014	15·495	0·0012	38·047	0·0030
30IV-D12-7	0·703018	0·000014	0·513106	0·000010	9·3	18·213	0·0010	15·493	0·0012	38·034	0·0032
Dragon Bone axial basalts											
30IV-D2-1	0·703256	0·000014	0·513012	0·000004	7·5	18·138	0·0004	15·549	0·0004	38·278	0·0012
30IV-D2-2	0·703266	0·000014	0·512997	0·000008	7·2	17·761	0·0008	15·472	0·0008	37·758	0·0024
30IV-D2-3	0·703353	0·000014				17·706		15·462		37·768	
Dragon Bone rift mountain											
21V-D2	0·702695	0·000016	0·513086	0·000006	8·9	17·865	0·0010	15·454	0·0010	37·648	0·0026

εNd were calculated using the Bulk Earth value of $^{143}Nd/^{144}Nd = 0·51263$ (Bouvier *et al.*, 2008).

Trace element fractionation

Incompatible element concentrations of the Dragon Flag basalts (type 1 and type 2) increase linearly with MgO, consistent with magmatic differentiation (Fig. 8). The Dragon Bone rift mountain basalt plots close to the Dragon Flag segments on a REE vs MgO diagram. However, the Dragon Bone axial basalts form a cluster with higher concentrations of incompatible trace elements at lower MgO contents. Because of the limited numbers of Dragon Flag type 1 basalts and the Dragon Bone rift mountain basalt, the fractional crystallization and partial melting effects mainly concern the Dragon Bone type 2 basalts and the Dragon Bone axial basalts.

Clinopyroxene fractionation can increase the La/Yb and Zr/Sm ratios in the remaining melt because D_{La} and D_{Zr} values are lower than those of D_{Yb} and D_{Sm}, respectively, for clinopyroxene/melt (Green *et al.*, 2000). The Dragon Flag type 2 basalts are characterized by a relatively steep slope of La/Yb vs La (or Yb) with La at a lower range (1·5–2·43 ppm, La = 2·43 in sample 30IV-TVG4-7) and a relatively flat slope at a higher La range (2·43–3 ppm) (Fig. 8b and c). This indicates that partial melting and fractional crystallization are different for the two slopes of the Dragon Flag basalts.

We modeled the partial melting and fractionation crystallization processes to evaluate their influences on the Dragon Flag type 2 samples. The partial melting trends are modeled through fractional melting of two different sources and the fractionation crystallization processes are mainly concerned with the influence of crystallization of clinopyroxenes (Fig. 8a–c). Two modeled fractional partial melting trends are shown for comparison, one of a depleted MORB mantle source and the other from a residue of a metasomatized mantle (Fig. 8a and c). It is obvious that partial melting from a DMM source cannot explain the trend of either the Dragon Flag or the Dragon Bone basalts (Fig. 8a and c). A previously depleted metasomatized mantle is more appropriate as the source for the Dragon Flag type 2 basalts with La < 2·43 ppm. The basalts with La < 2·43 ppm are generated by higher degrees of partial melting than basalts with La > 2·43 ppm. The latter have sustained lower degrees of partial melting, which was supposed to be generated at shallower depth, and thus are more likely to have experienced low-pressure fractional crystallization during migrating to the seafloor, in agreement with the modeled low-pressure fractional crystallization (Fig. 8a–c).

Despite the effects of partial melting and fractional crystallization on the Dragon Flag type 2 basalts compositions, the lavas vary in a narrow range of La/Yb (0·4–0·8) and Zr/Sm ratios (23–25) over a wide MgO range from 9·03 to 7·07 wt% (Fig. 8). This is consistent with the earlier explanation derived from major elements that the effect of clinopyroxene fractionation on the compositions of the Dragon Flag type 2 basalts is insignificant. The elevated La/Yb and Zr/Sm ratios of Dragon Bone axial basalts around 6·20 wt% MgO indicate that clinopyroxenes fractionate at higher pressures in the Dragon Bone axial lavas prior to eruption.

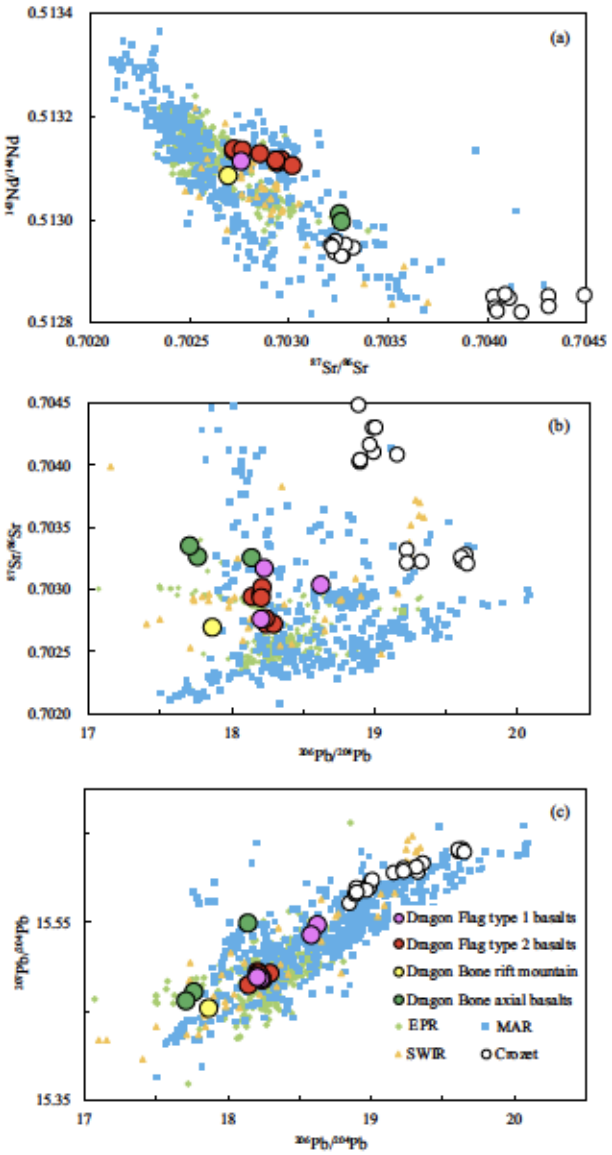

Fig. 6. Variations of (a) $^{87}Sr/^{86}Sr$ vs $^{143}Nd/^{144}Nd$, (b) $^{206}Pb/^{204}Pb$ vs $^{87}Sr/^{86}Sr$ and (c) $^{206}Pb/^{204}Pb$ vs $^{207}Pb/^{204}Pb$ of the Dragon Flag and Dragon Bone basalts, compared with the Crozet hotspots (Salters & White, 1998; Breton *et al.*, 2013) as well as basalts from the EPR, MAR and SWIR.

Despite the fractionation of clinopyroxene, the La/Yb and Zr/Sm ratios were increased only in a very limited range at <50% clinopyroxene fractionation as shown in Fig. 8d and e. Thus, to explain the large difference of trace element ratios between the Dragon Bone and Dragon Flag basalts requires consideration of additional processes such as partial melting, source heterogeneities or mixing and assimilation. Modeled variations of trace element ratios by varying the degree of partial melting from a single mantle source cannot explain both the Dragon Bone axial basalts and the Dragon Flag basalts. Source composition variations are a more likely explanation.

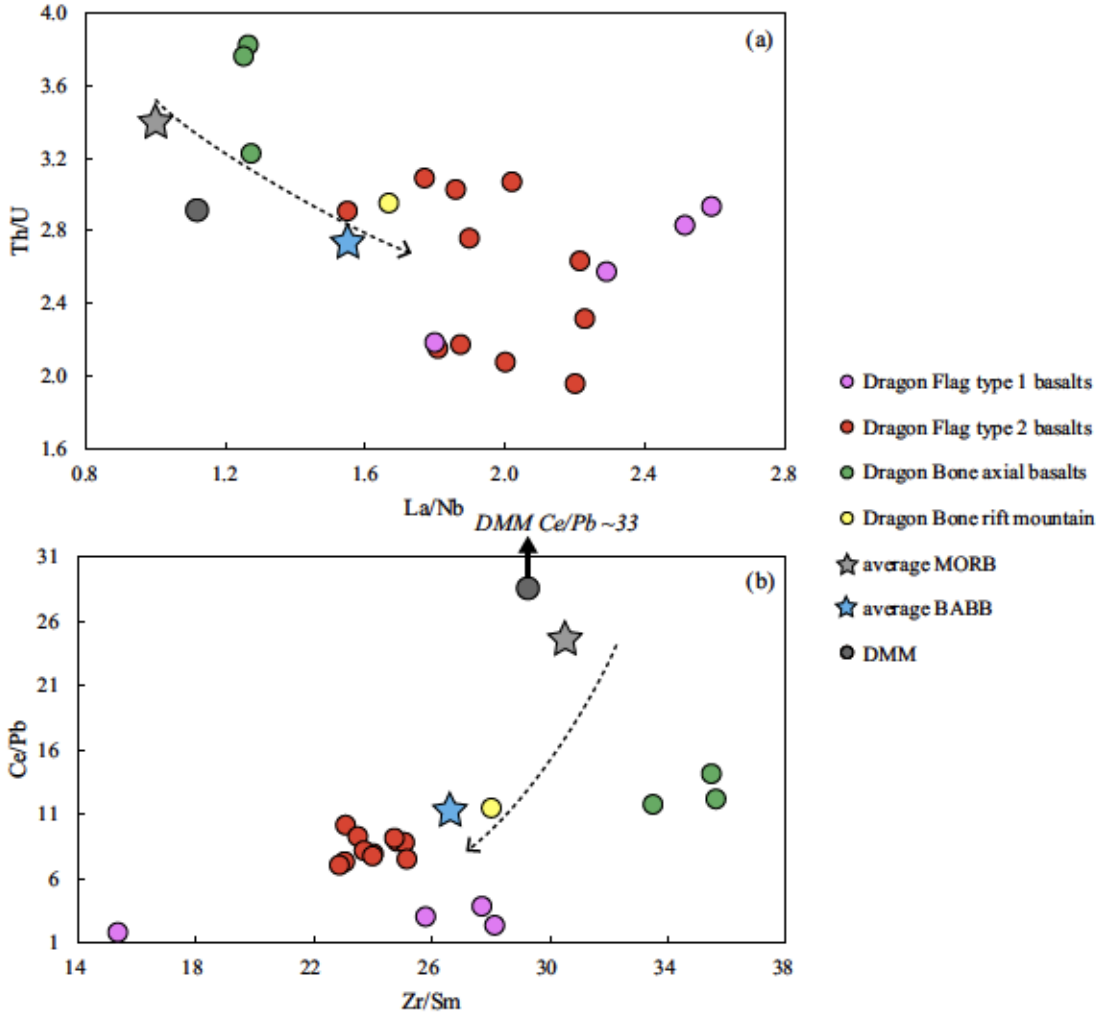

Fig. 7. (a) Th/U vs La/Nb and (b) Ce/Pb vs Zr/Sm of the Dragon Flag type 1 and type 2 basalts, the Dragon Bone axial and rift mountain basalts, compared with the average MORB and BABB values (Gale *et al.*, 2013) and DMM composition from Salters & Stracke (2004). The arrow signifies the direction from MORB to BABB, which indicates how these trace element ratios vary when affected by fluid.

Major elements insights into source variations

The variations in the $Na_{8.0}$–$Fe_{8.0}$ system are mainly affected by the differences in melting processes (Klein & Langmuir, 1987) or by mantle composition variations (Dick & Zhou, 2015). The Dragon Flag (type 1 and type 2) basalts plot at the low-sodium, high-iron end of the global MORB array (Fig. 9) indicating that they represent either melts from a high degree of mantle melting (Klein & Langmuir, 1987) or melts from a more depleted source than the MORB source mantle (Dick & Zhou, 2015). The Dragon Bone rift mountain basalt plots more towards the middle of the global trend, indicating either a moderately less depleted mantle source or lower degrees of mantle melting. In either case, they lie at the end of a systematic trend of decreasing $Na_{8.0}$ and increasing $Fe_{8.0}$ from the Rodriguez Triple Junction to the Marion Platform as previously noted by Dick & Zhou (2015). Given the thin crust over the Marion Rise and their depleted trace element patterns, the best explanation for the Dragon Flag composition is an increasingly refractory mantle source (Zhou & Dick, 2013; Dalton *et al.*, 2014; Dick & Zhou, 2015). This explanation is consistent with the previous conclusion that it is the source variations, rather than partial melting, that account for their elemental differences.

The Dragon Bone axial lavas, on the other hand, plot at the high-$Na_{8.0}$ low-$Fe_{8.0}$ end, which indicates either a low degree of melting or a fertile mantle source. Given the highly depleted composition of the mantle peridotites across the Dragon Bone Segment and the adjacent rift mountains (Zhou & Dick, 2013; Gao *et al.*, 2016; Wang *et al.*, 2019), the logical explanation for these lavas is that they represent extremely low degrees of melting of a depleted mantle matrix containing enriched components, and thus largely sample the enriched rather than the depleted component.

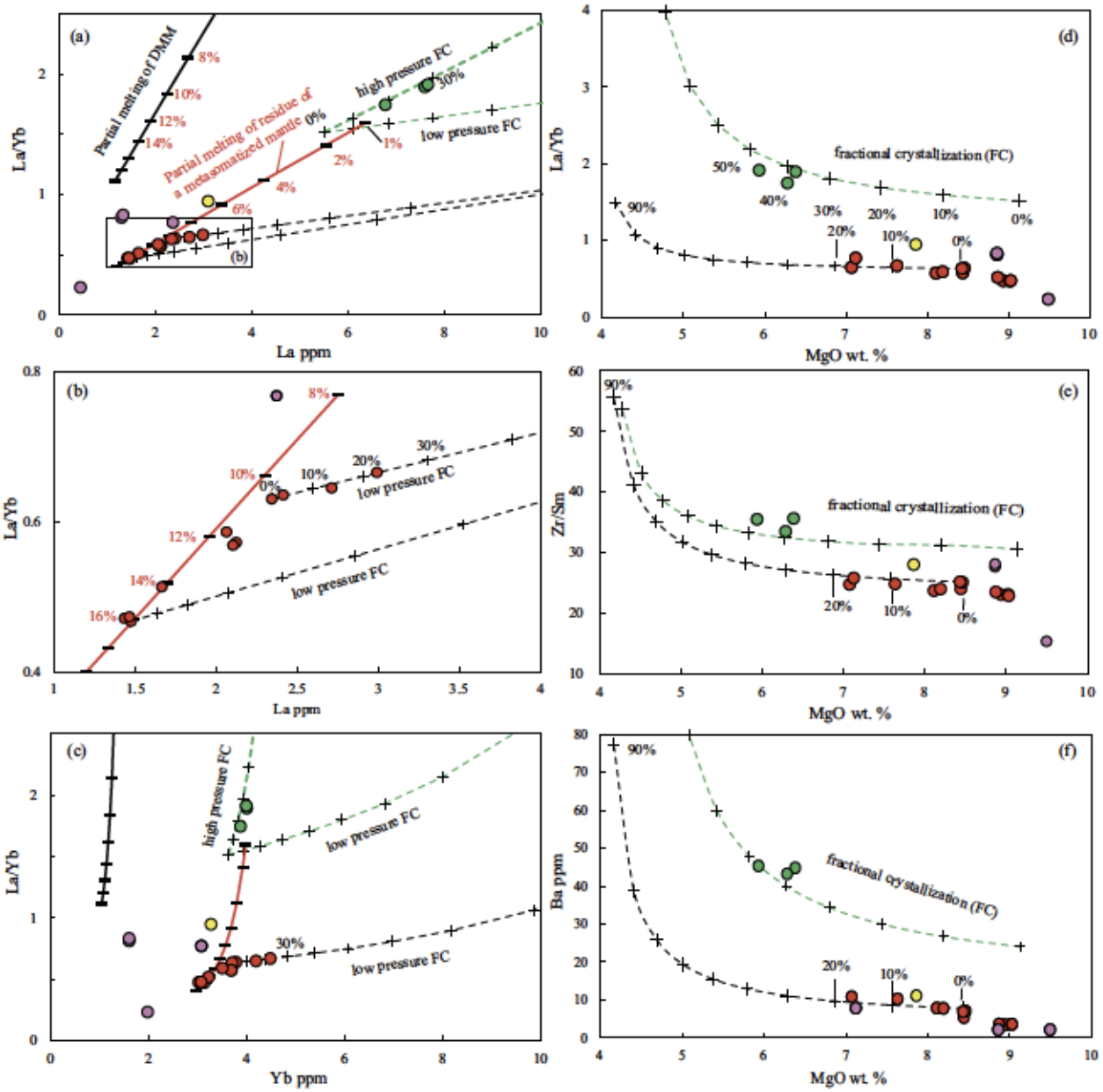

Fig. 8. Potential influence of clinopyroxene crystallization on the Dragon Flag basalts and the Dragon Bone axial basalts, shown by selected trace element ratios vs trace elements (a–c) and MgO contents (d–f): (a) La/Yb vs La; (b) magnification of the rectangle in (a); (c) La/Yb vs Yb; (d) La/Yb vs MgO; (e) Zr/Sm vs MgO; (f) Ba vs MgO. The fractionation begins where clinopyroxenes crystallize (green and black dashed lines). In (a) two partial melting trends, one starting from a common MORB mantle source (Salters & Stracke, 2004; black line) and the other starting from residue of a metasomatized mantle (red line), are shown for comparison, both labelled with degrees of partial melting. Partition coefficients for La, Yb, Zr, Sm and Ba are taken from Green *et al.* (2000) and MgO from Liu *et al.* (2008). Symbols as in Fig. 2.

Trace element ratios reveal a mantle more depleted than DMM

We have shown that trace element ratio variations of the Dragon Flag type 2 basalts are mainly controlled by partial melting and fractional crystallization processes, and the large gap between the Dragon Flag and Dragon Bone axial basalts is probably related to source composition difference. Additionally, their major and trace element contents as well as the isotopic compositions of the Dragon Flag type 2 and the Dragon Bone axial basalts show correlated variations. Dragon Bone axial basalt variation lies at the extension of the Dragon Flag basalt variation; examples are shown in Fig. 10. In general, trace element ratios with the more incompatible element in the numerator correlate negatively with $^{143}Nd/^{144}Nd$ and $^{206}Pb/^{204}Pb$ and positively with

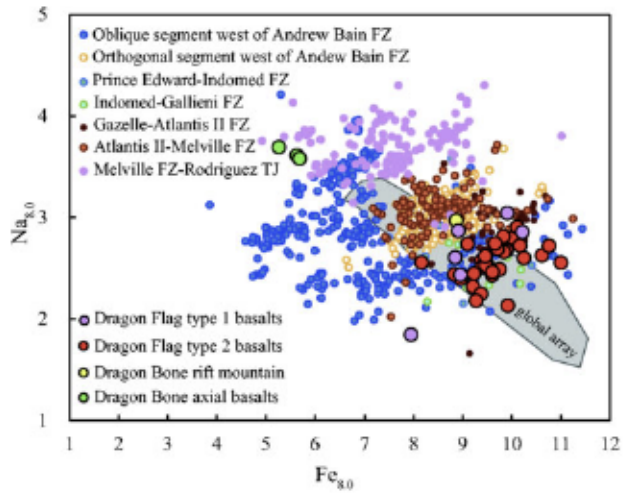

Fig. 9. Na_2O and FeO contents in weight per cent corrected for fractionation to 8 wt% MgO ($Na_{8.0} = Na_2O + 0.373MgO - 2.98$, $Fe_{8.0} = FeO + 1.664MgO - 13.313$; after Klein & Langmuir, 1987). Grey field is for the global trend of averaged MORB from Klein & Langmuir (1987). Here we use un-averaged data to highlight the progressive change in basalt chemistry.

$^{87}Sr/^{86}Sr$ (Fig. 10). As isotopic ratios are dependent only on source variations, these phenomena imply that the Dragon Bone axial basalts and Dragon Flag type 2 basalts share a mantle component.

The isotopically depleted Dragon Flag type 2 basalts have trace element ratios that are extreme with La/Nb up to 2·2 and Ce/Pb down to seven compared with the average MORB values of La/Nb (1·0) and Ce/Pb (26) (Fig. 7). Similarly, the low values for Th/U (2·0), La/Sm (0·6) and Sm/Yb (0·79) are much lower than the average MORB values of 3·4, 1·4 and 1·05 respectively. Additionally, the trace element ratios of the Dragon Flag basalts are lower than those of the MORB source mantle (Salters & Stracke, 2004). For example, Th/U and La/Sm ratios of the MORB source mantle are 2·9 and 0·87, whereas the averages of the Dragon Flag basalts are down to 2·5 and 0·68 respectively. The Dragon Flag basalts have experienced a high degree of melting; however, a high degree of melting of an average MORB mantle source cannot explain their lower than average MORB source Th/U and La/Sm ratios, but requires a source more depleted than the average MORB source.

A higher degree of melting for the Dragon Flag Segment compared with its adjacent Dragon Bone Segment has been proposed by Sauter *et al.* (2009), Li *et al.* (2015) and Niu *et al.* (2015) based on bathymetry and magnetic and gravity measurements. The Dragon Bone Segment is magma starved and although the degree of melting of the Dragon Flag is higher than that of the Dragon Bone Segment, the crust is still thin relative to normal ridges (Zhao *et al.*, 2013). Thus a source more depleted than the average MORB source beneath the two ridge segments is likely from both geochemical and geological perspectives.

Dragon Flag basalt source

Dragon Flag type 1 basalt source

Mainly two scenarios have been proposed in the literature for the possible sources of the Dragon Flag type 1 basalts. One is influence by the Crozet hotspot (Breton *et al.*, 2013; Yang *et al.*, 2017) and the other is subduction-modified subarc mantle (Li *et al.*, 2017). Below we will discuss the two possible origins for the sources of the trace element depleted but isotopically enriched Dragon Flag type 1 basalts.

Sauter *et al.* (2009) considered the off-axis shallow ocean floor along the Dragon Flag Segment region as relicts of a volcanic plateau caused by a sudden increase of the magma supply over the past 10 Myr that is still occurring at segment 27. This melting anomaly may be ascribed to a regionally higher mantle temperature provided by mantle migration from the Crozet hotspot towards the SWIR Sauter *et al.* (2009). Zhao *et al.* (2013) discovered that the shallow ocean floor is formed by uplifted oceanic core complexes with relatively thin basaltic crust indicating limited melt production.

Breton *et al.* (2013) proposed that the shallow mantle beneath the Dragon Flag Segment is contaminated by Crozet plume materials based on Sr–Nd–Pb–He isotopic compositions of basalts from the Crozet Archipelago, although they pointed that MORB from the Dragon Flag area do not display OIB-like trace element signature, nor do they show any direct affinity to Crozet basalts (Breton *et al.*, 2013). Yang *et al.* (2017) found isotopic evidence for the influence of the Crozet hotspot from basalts from only the segment 27 ridge axis. Because the isotopic compositions of the Dragon Flag basalts are in the MORB field and because the Crozet data fall at the extension of the MORB field in Sr–Nd–Pb space (Fig. 6), it is difficult to distinguish between variation within the MORB field and contamination with the Crozet plume. Given that the Crozet hotspot is 1000 km off-ridge, and Crozet has a small plume flux, it is unlikely that it would affect one segment only from that distance.

The depleted trace element signature of the Dragon Flag type 1 basalts argues against hotspot influence. Yang *et al.* (2017) argued that the Crozet plume material would travel along the lithosphere–asthenosphere boundary from the plume towards the ridge. During this transport the plume material would undergo decompression melting. When it arrives at the MOR the plume material melts again, thus producing MORB low in incompatible trace elements but with enriched isotopic compositions. However, these isotopically enriched Dragon Bone type 1 basalts are among the most depleted D-MORB; that is, more depleted than can be generated from a N-MORB source. It is unlikely that such depleted melts are formed by a low degree of melting of a geochemically enriched plume-related material.

The $^{87}Sr/^{86}Sr$–$^{143}Nd/^{144}Nd$ variations of the Dragon Flag type 2 basalts trend towards the east Crozet hotspot. However, in the $^{206}Pb/^{204}Pb$–$^{87}Sr/^{86}Sr$ space (Fig. 6) it is clear that both west and east Crozet basalts

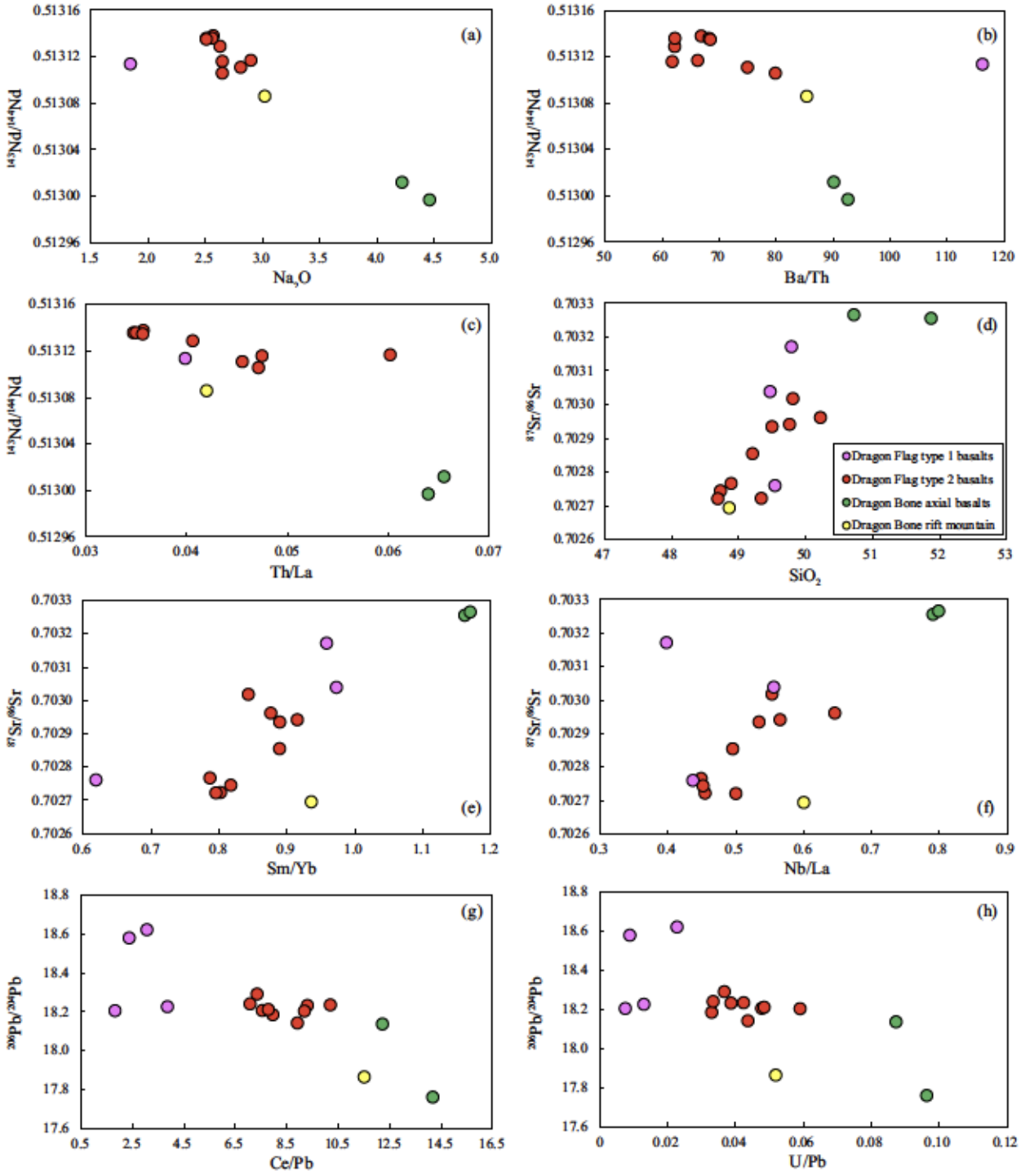

Fig. 10. Variation of isotopic compositions with selected major elements and trace element ratios of the Dragon Flag type 1 and type 2 basalts, the Dragon Bone axial and rift mountain basalts: (a) $^{143}Nd/^{144}Nd$ vs Na_2O; (b) $^{143}Nd/^{144}Nd$ vs Ba/Th; (c) $^{143}Nd/^{144}Nd$ vs Th/La; (d) $^{87}Sr/^{86}Sr$ vs SiO_2; (e) $^{87}Sr/^{86}Sr$ vs Sm/Yb; (f) $^{87}Sr/^{86}Sr$ vs Nb/La; (g) $^{206}Pb/^{204}Pb$ vs Ce/Pb; (h) $^{206}Pb/^{204}Pb$ vs U/Pb.

cannot contribute significantly to the Dragon Bone and Dragon Flag basalts.

Another proposed origin for the Dragon Flag type 1 basalts is from remnants of subarc mantle; the peridotite mantle now beneath the central SWIR mantle is proposed to have undergone hydrous melting in mantle wedge conditions in the Neoproterozoic (Gao *et al.* 2016). Li *et al.* (2017) found that the H_2O contents of these Dragon Flag basalts are higher than those of most N-MORB. Their high H_2O contents are similar to those of OIB and back-arc basin basalt (BABB) and the high H_2O/Ce ratios in the Dragon Flag basalts are probably

the result of arc-related hydrous components in the mantle source (Li *et al.*, 2017).

The trace elements of the Dragon Flag type 1 basalts are depleted in fluid-immobile elements Nb, Ta and Zr and enriched in fluid-mobile elements Ba, Sr and Pb (Fig. 5a). These signatures are typical for fluid addition in an arc mantle setting of lower Zr/Sm, Th/U, Ce/Pb and higher La/Nb ratios than the average BABB (Gale *et al.*, 2013) (Fig. 7). For the Dragon Flag type 1 basalts Pb and Sr are enriched over Nd and Hf, consistent with the influence of fluid addition to the source (Fig. 5), and these basalts have high Ba/La at very low Th/Yb (Fig. 11) ; all these features are consistent with slab fluid addition.

If the Dragon Flag type 1 source originated in the subarc then it has experienced multi-stage, at least two, depletions, one at the subarc setting and one recently beneath the mid-ocean ridge. A hydrous fluid-metasomatized mantle can melt to a greater extent under hydrous subarc conditions before its entrainment to beneath the mid-ocean ridge, because fluid flux would lower its solidus temperature (e.g. Davies & Bickle, 1991; Hirose & Kawamoto, 1995; Gaetani & Grove, 1998), thus producing a very refractory melting residue (e.g. Parkinson & Pearce, 1998; Gao *et al.*, 2016). Such a refractory residue can generate more depleted melt during the subsequent melting at the mid-ocean ridge and produce basalts more depleted than the global MORB. The multi-stage depletions of a fluid-metasomatized mantle would erase the incompatible elements to a lesser level than the real arc basalts but still retain the typical fluid addition signatures.

Given the considerations above, we propose that the source for the Dragon Flag type 1 basalts is more likely to find its origin in a subduction setting rather than from deep hotspot materials.

Composition of the fluid

Mafic crust and sediments are two major components of a slab. We found that the fluid flux from oceanic crust alone cannot explain the strong Pb and Sr peaks of the Dragon Flag type 1 basalts. Fluid flux derived from subducting oceanic crust with 0·57 ppm Pb and 129 ppm Sr will have a maximum of 0·50 ppm Pb and 52·63 ppm Sr during subduction modification using the Pb (88%) and Sr (41%) mobilities after Kogiso *et al.* (1997). After the metasomatism and multistage depletions, such Pb and Sr levels will result in a high Nd/Pb and Nd/Sr similar to N-MORB. To match the enrichments of Pb and Sr requires about 5 ppm Pb and 130 ppm Sr in the slab fluid (see calculation below). Considering the elements mobilities during subduction modification, sediment becomes the logical component from which fluid is also extracted, as it has high concentrations of Pb (20 ppm) and Sr (350 ppm) (Kimura *et al.*, 2009).

We have modeled the trace elements of the Dragon Flag type 1 basalts (Fig. 12 and Supplementary File S1). Calculations show that the source of the Dragon Flag type 1 basalts is consistent with an initial composition that is similar to bulk silicate Earth (BSE) (Sun & McDonough, 1989) or DMM (Salters & Stracke, 2004) that has seen a 10–20% fluid addition from subducted basaltic oceanic crust [average MORB data from Gale *et al.* (2013)] and sediment followed by 6–8% dynamic melting (Brunelli *et al.*, 2006) at a critical mass porosity of 2%. To generate the Dragon Flag type 1 basalts at segment 27, ~6% fractional melting is required and for the most depleted sample, 30IV-TVG4-2, a higher degree of fractional melting, ~10%, is needed. Fluid composition from the mafic part of oceanic crust was calculated using the mobility coefficients of Kogiso *et al.* (1997), whereas the Sr and Pb concentrations of the sediment-derived fluid were calculated using the mobility coefficients from Kimura *et al.* (2009). Melting parameters were taken from Salters & Longhi (1999) and Salters *et al.* (2002) and melting is modeled as melting of peridotite in the spinel stability field; that is, garnet-absent, as the melting is modeled for a subarc environment.

Dragon Flag type 2 basalt source

Using the same trace element ratios that indicate fluid addition of the Dragon Flag type 1 basalts, we found that the Dragon Flag type 2 basalts show much smaller Nb and Zr depletions than the type 1 basalts. Also they show lower Zr/Sm, Th/U and Ce/Pb and higher La/Nb ratios than the average MORB and BABB values (Fig. 7), together with their relatively high Ba/La at a very low Th/Yb (Fig. 11), indicating the addition of slab-derived fluid. It should be noted that the absolute trace element abundances are higher in the type 2 than in type 1 basalts at the same MgO contents (Fig. 4), so their difference is not due to fractional crystallization process but to discrepancies in their sources. Because the Dragon Flag type 2 basalts source cannot be as depleted as the type 1 source, the trace element ratios that indicate fluid addition in type 1 basalts are more prominent than in the type 2 basalts. The most logical component we added in the type 2 source is the subducted oceanic crust. We tested whether adding oceanic crust to the type 1 source (fluid + DMM or fluid + BSE) could result in trace element patterns with similar HFSE and heavy rare earth element (HREE) abundances to the Dragon Flag type 2 basalts. The result shows that by keeping the same critical porosity and the same degrees of partial melting in the arc mantle setting, we can model the trace elements patterns of the type 2 basalts by adding 11% of oceanic crust in the type 1 source. The calculations show that the initial subarc mantle requires 11% addition of recycled oceanic crust and 9% fluid addition to DMM. The fluid composition is modified from the oceanic crust using mobility coefficients of Kogiso *et al.* (1997). The final trace element pattern of the modeled melt is shown in Fig. 12 and the details of the calculations are provided in Supplementary File S1.

We realize that the two models for the Dragon Flag basalts are highly non-unique and that there are other scenarios that would also be consistent with the data. However, they are the 'simplest' models that can

explain the basalt compositions and there are some limits to the model. Irrespective of the exact lithology from which the fluid is derived, whether it is basaltic crust, as modeled here, or bulk oceanic crust including sediments, the trace element characteristics (i.e. fluid-mobile over -immobile elements) become too high if more than 20% of fluid is added to a BSE-like or more depleted source. For example, by assuming that the fluid is derived from the basaltic crust, our calculations estimate that (1) the amount of slab fluid and (2) the timing of recycling subducted crust and (3) the timing of the subarc depletion event should respectively be in the following ranges: (1) 1–20%, (2) 1·5–0·9 Ga, which is long before the assembly of the Gondwana (550 Ma), and (3) 0·7–0·2 Ga, before the opening of the SWIR (Fig. 13). A single calculation procedure (Supplementary File S2) is modified after Stracke *et al.* (2003) and the whole calculation process is done using Matlab (code in Supplementary File S3). The amount of slab fluid added in the subarc mantle cannot be more than 20%, otherwise the final isotopic composition cannot fit all three isotopic systems (Supplementary File S2). The results of the modeling suggest that the subsequent depletion of this fluid-metasomatized subarc mantle has to take place relatively late (500–900 Ma) after the fluid addition to accumulate enough ingrowth of isotopic signatures given that the ancient recycled oceanic crust and sediments are low in $^{87}Sr/^{86}Sr$, $^{143}Nd/^{144}Nd$ and $^{206}Pb/^{204}Pb$ relative to the modern values (e.g. Rehkämper & Hofmann, 1997); otherwise once the subarc depletion happened, the Sm/Nd, Rb/Sr and U/Pb ratios in the residual subarc mantle would be too low to make any significant isotopic ingrowth before the final mid-ocean ridge depletion.

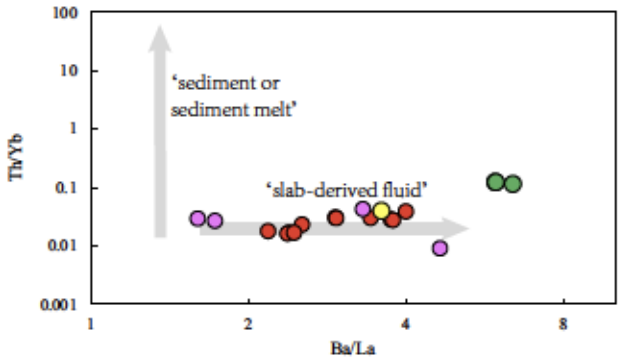

Fig. 11. The relatively high Ba/La ratios of the Dragon Flag (type 1 and type 2) basalts, and the Dragon Bone axial and rift mountain basalts at very low Th/Yb indicating the involvement of slab-derived fluid (Elliott *et al.*, 1997; Woodhead *et al.*, 2001). Symbols as in Fig. 2.

Dragon Bone axial basalt source

In Sr–Nd isotopes space the Dragon Bone axial basalts lie at the extension of the Dragon Flag type 2 basalts forming a trend that is rooted in the field for Indian MORB but extends to low $^{143}Nd/^{144}Nd$ and high $^{87}Sr/^{86}Sr$ ratios (Fig. 14).

In the $^{208}Pb/^{204}Pb$ and $^{207}Pb/^{204}Pb$ vs $^{206}Pb/^{204}Pb$ space (Fig. 14), the Dragon Bone axial basalts have higher $^{207}Pb/^{204}Pb$ and $^{208}Pb/^{204}Pb$ than Dragon Flag basalts at given $^{206}Pb/^{204}Pb$ and overlap with the field of the Ejeda–Bekily dike compositions. Considering the short half-life of ^{235}U, this requires an ancient enrichment in U/Pb in Dragon Bone mantle source older than 1 Ga, before the SWIR existed (Patriat & Segoufin, 1988). The Ejeda–Bekily dikes are sourced in Madagascar SCLM in Archean–Proterozoic times (Mahoney *et al.*, 1991; Storey *et al.*, 1997) and thus the ancient age

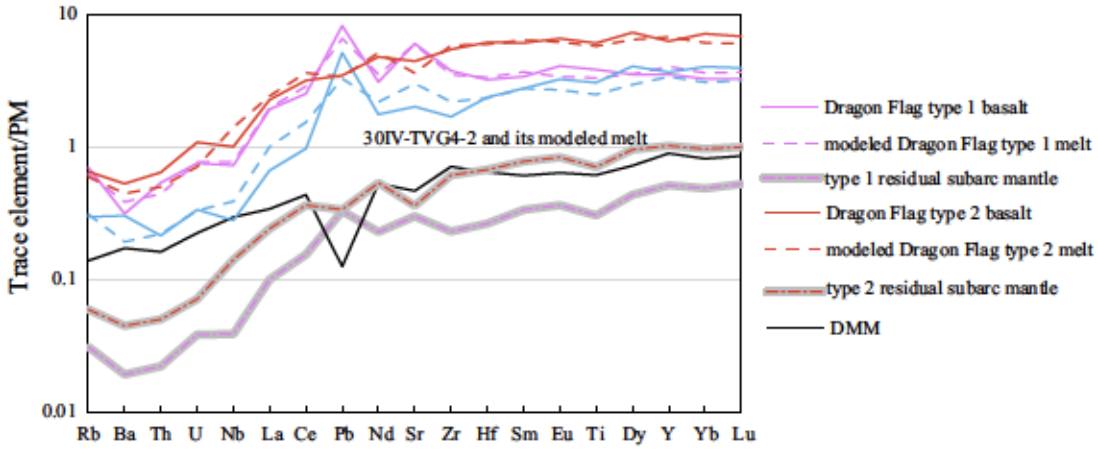

Fig. 12. Primitive mantle normalized trace element patterns of the modeled melts (dashed lines) by two-stage depletion of a subarc mantle that had been affected by slab–fluid addition, compared with the most primitive basalts in each type of basalt (continuous lines). The continuous purple line is the most primitive Dragon Flag type 1 basalt represented as the average of samples 30IV-D13-1 and 34III-TVG5-1, which have primitive MgO contents. The continuous blue line is sample 30IV-TVG4-2, which also has a very primitive MgO but was generated by different degrees of partial melting from the purple line. The red line indicates the most primitive Dragon Flag type 2 basalts represented by sample 30IV-D8-2, which has the most primitive MgO. Trace element patterns of the residual subarc mantle after subarc depletion for each type of Dragon Flag basalt are shown in grey shaded dash–dot lines colored in red and purple. They are more depleted than the common MORB source DMM (Salters & Stracke, 2004). Detailed modeling processes are discussed in the text and provided in Supplementary File S1.

of SCLM is suitable as a source component for the Dragon Bone axial basalts. In addition, the Dragon Bone axial basalts have Nb/Ta = 17 and Zr/Hf = 45–47, on the edge of the field of continental basalts of Nb/Ta = 16·4–18·8 and Zr/Hf= 40·6–43·7 that was sourced from SCLM (Münker *et al.*, 2003) . Consistently, the relatively enrichment of Ba, Nb, Ta, K, La, Sr and Zr and depletion in Pb and Ti of the Dragon Bone axial basalts are similar to the trace element patterns of some types of metasomatized peridotite xenoliths from the SCLM; for example, Ejeda–Bekily dikes (Fig. 4) (Mahoney *et al.*, 1991, 2008; Dostal *et al.*, 1992).

Simple mixing calculations show that the trend of the Dragon Bone axial basalts can be reproduced by mixing of an enriched component that was sourced from the SCLM—the average composition of the Ejeda–Bekily dikes or the average composition of 39–41°E SWIR basalts—with the most isotopically depleted Dragon Flag type 2 basalt (Figs 14 and 15) in isotopic and trace element ratios. Calculations show that their $^{87}Sr/^{86}Sr$, $^{143}Nd/^{144}Nd$ and $^{206}Pb/^{204}Pb$ variations can be modeled by adding about 10–20% SCLM into the isotopically most depleted Dragon Flag type 2 basalt (Fig. 14a–c). Or, as supported by their trace element and isotopic ratios, the Dragon Bone axial basalts permit ~10% contribution of the SCLM as shown by $^{143}Nd/^{144}Nd$, $^{87}Sr/^{86}Sr$, Ce/Pb, La/Th and La/Nb (Fig. 15). The calculation process is documented in Supplementary File S4.

The recycling of SCLM could have occurred either during the breakup of Gondwana or as a result of an earlier event during formation and accretion of Neoproterozoic island arc terranes during the subduction of the Mozambique Ocean. The presence of ancient SCLM merits further studies, such as measuring $^{187}Os/^{188}Os$, as SCLM is thought to be characterized by lower $^{187}Os/^{188}Os$ than the BSE value (Shirey and Walker, 1998; Pearson *et al.*, 2004).

Significance of recycled lithosphere at the central SWIR

The trace element ratios of the Dragon Flag basalts are lower than those of DMM, suggesting a mantle more depleted than DMM. We have proposed the subarc mantle as the source for the Dragon Flag basalts at the 200 km long Dragon Flag Segment, which is a significant part of the central SWIR.

The Dragon Bone axial basalts almost always lie at or near the extension of the Dragon Flag type 2 basalts (Figs 14 and 15), leading us to conclude that the Dragon Bone axial basalts originated from a similarly depleted mantle. In addition to the Dragon Flag source as a component in the source of the Dragon Bone basalts, based on the similarity with the Ejeda–Bekily dikes a component of delaminated lithosphere is proposed. This is most probably Archean SCLM beneath Gondwana, derived from beneath the Madagascar Plateau, a fragment of the East African Orogenic Belt (EAOB)—a

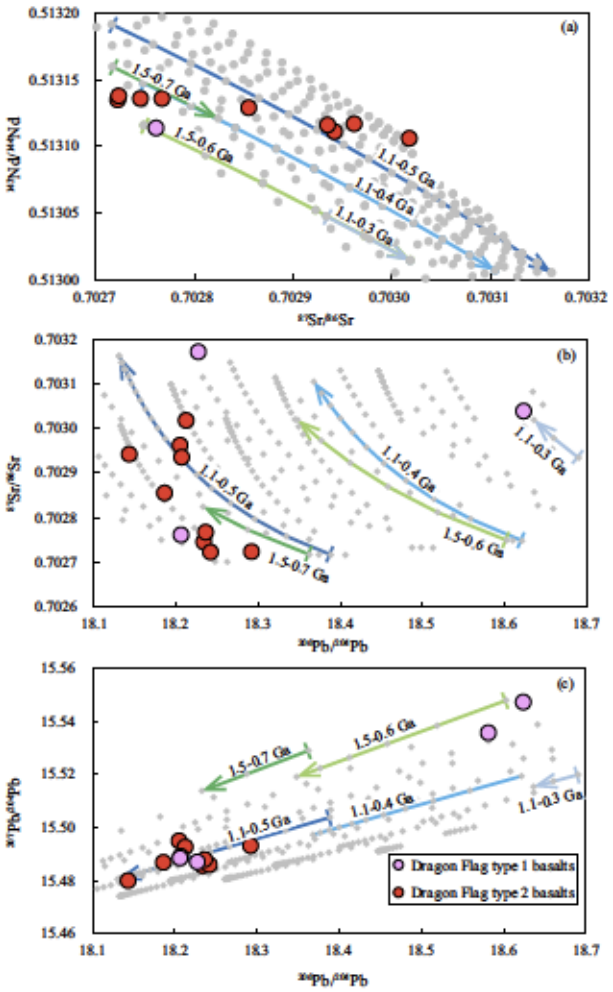

Fig. 13. Modeled present-day isotopic compositions (grey dots) in (a) $^{143}Nd/^{144}Nd$ vs $^{87}Sr/^{86}Sr$, (b) $^{87}Sr/^{86}Sr$ vs $^{206}Pb/^{204}Pb$, and (c) $^{207}Pb/^{204}Pb$ vs $^{206}Pb/^{204}Pb$ of the final melts by two-stage depletion of the slab–fluid metasomatized subarc mantle, compared with the Dragon Flag type 1 and type 2 basalts. The colored trends with arrows indicate how isotopic compositions evolve by increasing the amount of fluid at the specific ages of recycling of the bulk oceanic crust (1·1 and 1·5 Ga) and of the subarc depletion (0·3, 0·4, 0·5, 0·6 and 0·7 Ga). These five lines indicate that the earlier the recycling and subarc depletion occurred, the more radiogenic their $^{143}Nd/^{144}Nd$ and $^{207}Pb/^{204}Pb$ ratios and less radiogenic their $^{87}Sr/^{86}Sr$ ratios would be. Details of the modeling are given in the text. Modeled results are all listed in Supplementary File S2.

mixed Archaean–Proterozoic terrane—whose rifting had historically initiated the breakup of Gondwana and formed the central SWIR (Stern, 1994; Jacobs & Thomas, 2004).

The Madagascar Plateau was also the locus of major flood volcanism at 88 Ma (Torsvik *et al.*, 1998), which can be related to the mantle plume in the Late Cretaceous under Marion Island. The eastern region of the plateau appears to be underlain largely by old arc mantle from the EAOB (Jacobs & Thomas, 2004). Meyzen *et al.* (2007) considered the mantle beneath the Marion Platform to be fed directly by a deep mantle plume originating beneath southern Africa associated

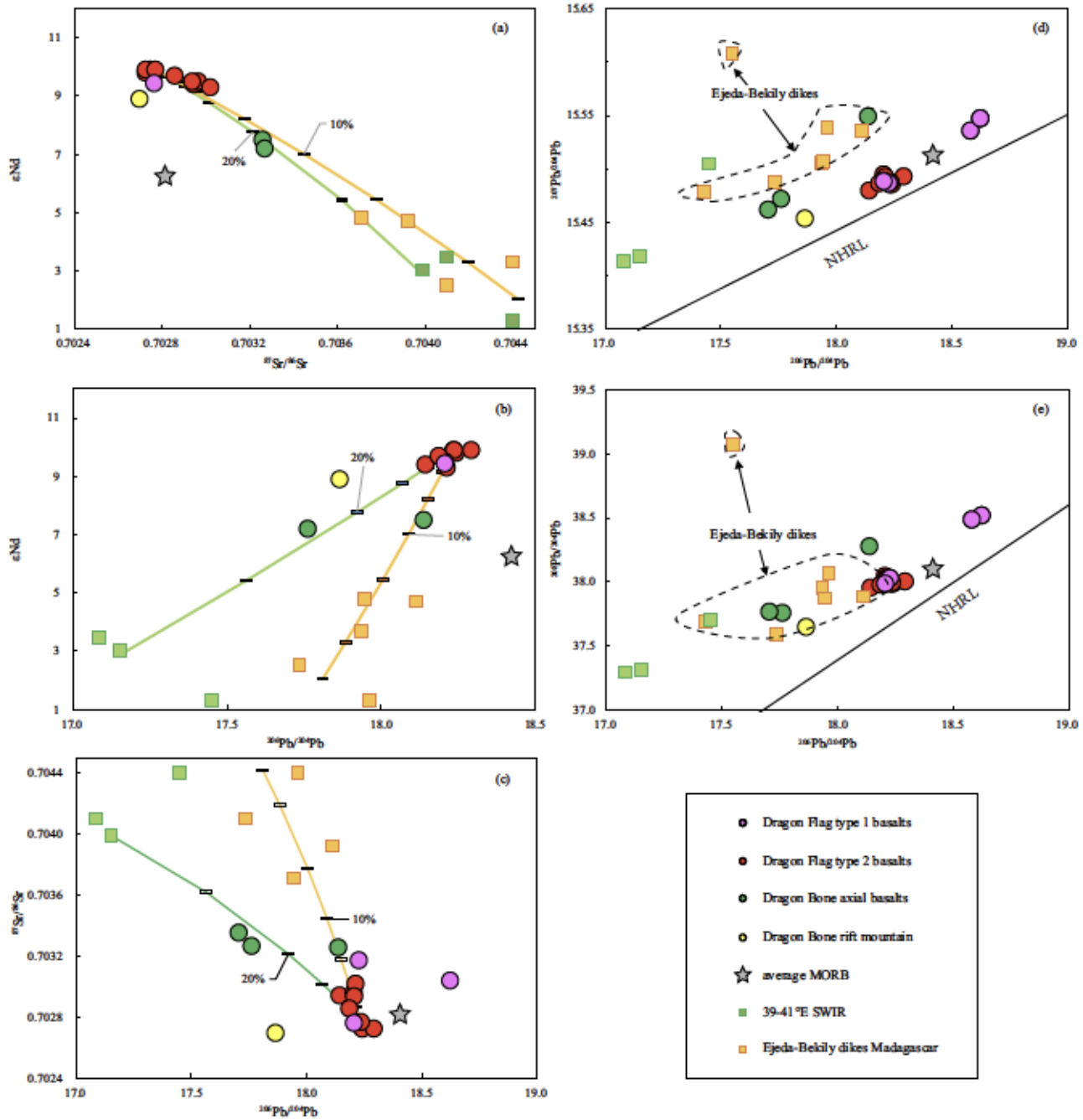

Fig. 14. Isotopic mixing of the most depleted Dragon Flag type 2 basalt (30IV-D8-2) with a composition of Ejeda–Bekily dikes (Mahoney *et al.*, 1991, orange lines) and a composition of basalts from the 39–41°E SWIR (Janney *et al.*, 2005). These data are also compared with the average MORB (Gale *et al.*, 2013). In (a)–(c), mixing lines are shown starting from the isotopically most depleted Dragon Flag type 2 basalt (30IV-D8-2) to a 39–41°E SWIR basalt composition (the green line) and average Ejeda–Bekily dikes composition (orange line), with mixing proportions in the sequences 0, 1, 2, 5, 10, 20, 50 and 100%. Mixing percentages are labelled next to the ticks. NHRL in (d) and (e) is the northern hemisphere reference line (Hart, 1984).

with the Karoo volcanic event at 180 Ma based on the upper mantle flow field of Behn *et al.* (2004). In contrast, the preferred model in this work suggests instead that the mantle source beneath the Marion Platform is delaminated Neoproterozoic lithospheric mantle entrained in that upper mantle flow.

CONCLUSIONS

Fresh basalt glasses recovered from the ultraslow-spreading Dragon Flag Magmatic Segment and the Dragon Bone Amagmatic Segment show differences in their major element, trace element and Sr–Nd–Pb isotope compositions. The Dragon Bone axial basalts

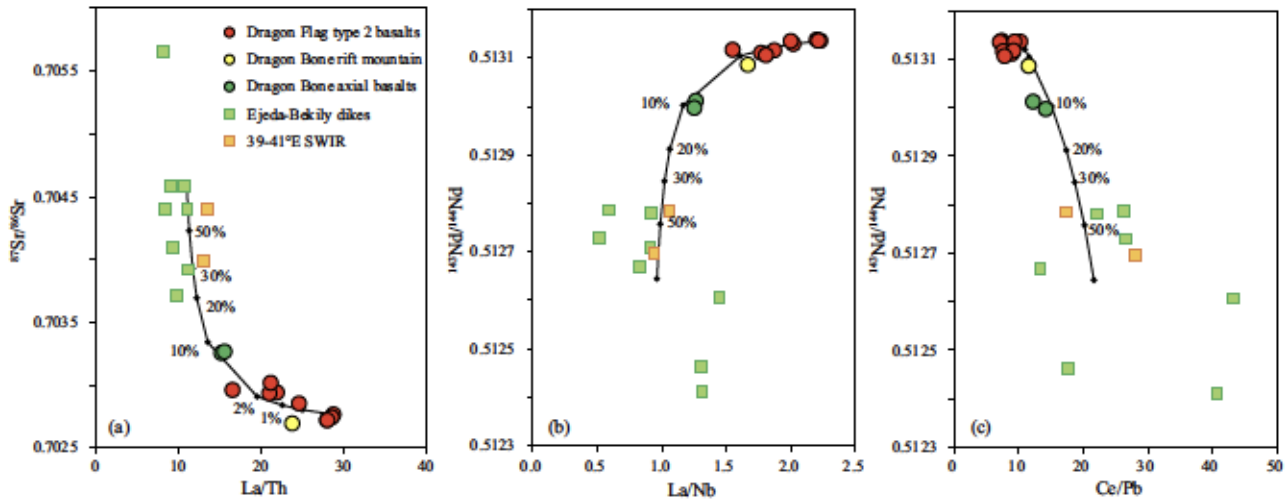

Fig. 15. Mixing of the isotopically most depleted Dragon Flag type 2 basalt (30IV-D8-2) with the average of the Ejeda–Bekily dikes (filled green squares) or the 39–41°E SWIR (filled orange squares). (a) $^{87}Sr/^{86}Sr$ vs La/Th; (b) $^{143}Nd/^{144}Nd$ vs La/Nb; (c) $^{143}Nd/^{144}Nd$ vs Ce/Pb. Dots on the mixing line (black line) represent 0·5, 1, 2, 10, 20, 30 and 50% of the assumed composition added to the selected Dragon Flag type 2 basalt. Ejeda–Bekily dikes compositions are from Dostal *et al.* (1992) and Mahoney *et al.* (1991), and the 39–41°E SWIR basalts are from Janney *et al.* (2005).

have relatively high $^{87}Sr/^{86}Sr$ and low $^{143}Nd/^{144}Nd$ but have trace element ratios that are more similar to average MORB than the Dragon Flag basalts. Trace element concentrations and ratios are correlated with isotopes indicating that Dragon Bone and Dragon Flag basalt trace element variation is caused by source variations. The source for the Dragon Flag basalts is thought to have a component of depleted subarc mantle as evidenced by enrichment of fluid-mobile over fluid-immobile elements. The depletion event in the subarc setting generated a mantle more depleted than the common MORB source. For the Dragon Bone axial basalts, with the consideration that (1) the ranges of their Pb isotopic compositions and their relative enrichment in Ba, Nb, Ta, K, La, Sr and Zr and depletion in Pb and Ti show resemblance to the Ejeda–Bekily dikes and (2) their Sr and Nd isotopic compositions together with Ce/Pb, La/Nb and La/Th ratios can be modeled by mixing between the average Ejeda–Bekily dikes and the most isotopically depleted Dragon Flag basalts, we propose that the Dragon Bone axial basalts, similar to these dikes, are sourced from subcontinental lithospheric Archean mantle, derived from beneath the Madagascar Plateau.

ACKNOWLEDGEMENTS

We express our gratitude to A. Sachi-Kocher, G. White, S. Yang, S. Henrick, B. Mayer and N. Waeselmann for their help in analyses at the National High Magnetic Field Laboratory, and Y. Liu and Y. Ai for major element analyses at the Analytical Laboratory of Beijing Research Institute of Uranium Geology. We very much appreciate the guidance of M. Humayun in data processing. We also thank the crew and scientists of RV *Dayang Yihao* Cruises 21, 30 and 34.

FUNDING

The RV *Dayang Yihao* cruises were supported by China Ocean Mineral Resources Research and Development Association (COMRA) and organized by Second Institute of Oceanography, SOA. This work was supported by the National Key R&D Program of China (2018YFC0309903), National Natural Science Foundation of China (NSFC 42006051) and Chinese National Key Basic Research Program (2012CB417300). H. Dick obtained partial support from the US National Science Foundation (NSF OCE MG&G #1434452), and the Woods Hole Oceanographic Institution. A portion of this work was performed at the National High Magnetic Field Laboratory, which is supported by the National Science Foundation Cooperative Agreement No. DMR-1644779 and the state of Florida.

SUPPLEMENTARY DATA

Supplementary data are available at *Journal of Petrology* online.

REFERENCES

Behn, M. D., Conrad, C. P. & Silver, P. G. (2004). Detection of upper mantle flow associated with the African Superplume. *Earth and Planetary Science Letters* **224**, 259–274.

Bouvier, A., Vervoort, J. D. & Patchett, P. J. (2008). The Lu–Hf and Sm–Nd isotopic composition of CHUR: constraints from unequilibrated chondrites and implications for the bulk composition of terrestrial planets. *Earth and Planetary Science Letters* **273**, 48–57.

Bown, J. W. & White, R. S. (1994). Variation of spreading rate of oceanic crustal thickness and geochemistry. *Earth and Planetary Science Letters* **121**, 435–449.

Breton, T., Nauret, F., Pichat, S., Moine, B., Moreira, M., Rose-Koga, E. F., Auclair, D., Bosq, C. & Wavrant, L.-M. (2013).

Geochemical heterogeneities within the Crozet hotspot. *Earth and Planetary Science Letters* **376**, 126–136.

Brunelli, D., Seyler, M., Cipriani, A., Ottolini, L. & Bonatti, E. (2006). Discontinuous melt extraction and weak refertilization of mantle peridotites at the Vema lithospheric section (Mid-Atlantic Ridge). *Journal of Petrology* **47**, 745–771.

Cannat, M., Rommevaux-Jestin, C., Sauter, D., Deplus, C. & Mendel, V. (1999). Formation of the axial relief at the very slow spreading Southwest Indian Ridge (49 to 69°E). *Journal of Geophysical Research: Solid Earth* **104**, 22825–22843.

Cannat, M., Sauter, D., Mendel, V. & Escartín, J. (2006). Large offset normal faults, ridge obliquity, and the distribution of volcanism at a melt-poor ultra-slow spreading ridge. *Eos Trans. AGU* 87(52), Abstract V11G-02.

Cannat, M., Sauter, D., Bezos, A., Meyzen, C., Humler, E. & Rigoleur, L. M. (2008). Spreading rate, spreading obliquity, and melt supply at the ultraslow spreading Southwest Indian Ridge. *Geochemistry, Geophysics, Geosystems* **9**, Q04002.

Chauvel, C. & Blichert-Toft, J. (2001). A hafnium isotope and trace element perspective on melting of the depleted mantle. *Earth and Planetary Science Letters* **190**, 137–151.

Chen, L., Chu, F.-Y., Zhu, J.-H., Dong, Y.-H., Yu, X., Li, Z.-G. & Tang, L.-M. (2015). Major and trace elements of abyssal peridotites: evidence for melt refertilization beneath the ultraslow-spreading Southwest Indian Ridge (53°E segment). *International Geology Review* **57**, 1715–1734.

Dalton, C. A., Langmuir, C. H. & Gale, A. (2014). Geophysical and geochemical evidence for deep temperature variations beneath mid-ocean ridges. *Science* **344**, 80–83.

Davies, J. H. & Bickle, M. J. (1991). A physical model for the volume and composition of melt produced by hydrous fluxing above subduction zones. *Philosophical Transactions of the Royal Society of London, Series A* **335**, 355–364.

DeMets, C., Gordon, R. G. & Argus, D. F. (2010). Geologically current plate motions. *Geophysical Journal International* **181**, 1–80.

Dick, H. J. & Zhou, H. (2015). Ocean rises are products of variable mantle composition, temperature and focused melting. *Nature Geoscience* **8**, 68–74.

Dick, H. J., Lin, J. & Schouten, H. (2003). An ultraslow-spreading class of ocean ridge. *Nature* **426**, 405–412.

Dostal, J., Dupuy, C., Nicollet, C. & Cantagrel, J. M. (1992). Geochemistry and petrogenesis of upper Cretaceous basaltic rocks from southern Malagasy. *Chemical Geology* **97**, 199–218.

Elliott, T., Plank, T., Zindler, A., White, W. & Bourdon, B. (1997). Element transport from slab to volcanic front at the Mariana arc. *Journal of Geophysical Research* **102**, 14991–15019.

Gaetani, G. A. & Grove, T. L. (1998). The influence of water on melting of mantle peridotite. *Contributions to Mineralogy and Petrology* **131**, 323–346.

Gale, A., Dalton, C. A., Langmuir, C. H., Su, Y. & Schilling, J. G. (2013). The mean composition of ocean ridge basalts. *Geochemistry, Geophysics, Geosystems* **14**, 489–518.

Gao, C., Dick, H. J., Liu, Y. & Zhou, H. (2016). Melt extraction and mantle source at a Southwest Indian Ridge Dragon Bone amagmatic segment on the Marion Rise. *Lithos* **246–247**, 48–60.

Green, T., Blundy, J., Adam, J. & Yaxley, G. (2000). SIMS determination of trace element partition coefficients between garnet, clinopyroxene and hydrous basaltic liquids at 2–7·5 GPa and 1080–1200 °C. *Lithos* **53**, 165–187.

Grove, TL, Kinzler, RJ, Bryan, WB, *Fractionation of Mid-Ocean Ridge Basalt (MORB)*, Mantle Flow and Melt Generation at Mid-Ocean Ridges Geophysical Monograph 71, Phipps Morgan, J, Blackman, DK, Sinton, JM, 281, 310,

Hart, S. R. (1984). The Dupal anomaly: a large-scale isotopic anomaly in the Southern hemisphere. *Nature* **309**, 753–757.

Hart, S. R. & Zindler, A. (1986). In search of a bulk-earth composition. *Chemical Geology* **57**, 247–267.

Hirose, K. & Kawamoto, T. (1995). Hydrous partial melting of lherzolite at 1 GPa: the effect of H_2O on the genesis of basaltic magmas. *Earth and Planetary Science Letters* **133**, 463–473.

Ito, G. & Mahoney, J. J. (2005). Flow and melting of a heterogeneous mantle: 1. Method and importance to the geochemistry of ocean island and mid-ocean ridge basalts. *Earth and Planetary Science Letters* **230**, 29–46.

Jacobs, J. & Thomas, R. J. (2004). Himalayan-type indenter-escape tectonics model for the southern part of the late Neoproterozoic–early Paleozoic East African–Antarctic Orogen. *Geology* **32**, 721–724.

Janney, P., Le Roex, A. & Carlson, R. (2005). Hafnium isotope and trace element constraints on the nature of mantle heterogeneity beneath the central Southwest Indian Ridge (13°E to 47°E). *Journal of Petrology* **46**, 2427–2464.

Jochum, K. P., Weis, U., Stoll, B., Kuzmin, D., Yang, Q., Raczek, I., Jacob, D. E., Stracke, A., Birbaum, K., Frick, D. A., Günther, D. & Enzweiler, J. (2011). Determination of reference values for NIST SRM 610–617 glasses following ISO guidelines. *Geostandards and Geoanalytical Research* **35**, 397–429.

Kimura, J.-I., Hacker, B. R., Keken, P. E. V., Kawabata, H., Yoshida, T. & Stern, R. J. (2009). Arc Basalt Simulator version 2, a simulation for slab dehydration and fluid-fluxed mantle melting for arc basalts: Modeling scheme and application. *Geochemistry, Geophysics, Geosystems* **10**, Q09004.

Kinzler, R. J. (1997). Melting of mantle peridotite at pressures approaching the spinel to garnet transition: application to mid-ocean ridge basalt petrogenesis. *Journal of Geophysical Research: Solid Earth* **102**, 853–874.

Klein, E. M. & Langmuir, C. H. (1987). Global correlations of ocean ridge basalt chemistry with axial depth and crustal thickness. *Journal of Geophysical Research* **92**, 8089–8115.

Kogiso, T., Tatsumi, Y. & Nakano, S. (1997). Trace element transport during dehydration processes in the subducted oceanic crust: 1. Experiments and implications for the origin of ocean island basalts. *Earth and Planetary Science Letters* **148**, 193–205.

Langmuir, C. H., Klein, E. M. & Plank, T. (1992). Petrological systematics of mid-ocean ridge basalts: constraints on melt generation beneath ocean ridges. In: Morgan, J. P., Blackman, D. K.& Sinton, J. M. (eds) *Mantle Flow and Melt Generation at Mid-Ocean Ridges. American Geophysical Union, Geophysical Monograph* **71**, 183–280.

Li, J., Jian, H., Chen, Y. J., Singh, S. C., Ruan, A., Qiu, X., Zhao, M., Wang, X., Niu, X., Ni, J. & Zhang, J. (2015). Seismic observation of an extremely magmatic accretion at the ultraslow spreading Southwest Indian Ridge. *Geophysical Research Letters* **42**, 2656–2663.

Li, W., Jin, Z., Li, H. & Tao, C. (2017). High water content in primitive mid-ocean ridge basalt from Southwest Indian Ridge (51·5°E): implications for recycled hydrous component in the mantle. *Journal of Earth Science* **28**, 411–421.

Lissenberg, C. J. & Dick, H. (2008). Melt–rock reaction in the lower oceanic crust and its implications for the genesis of mid-ocean ridge basalt. Earth and Planetary Science Letters **271**, 311–325.

Liu, Y., Gao, S., Kelemen, P. B. & Xu, W. (2008). Recycled crust controls contrasting source compositions of Mesozoic and Cenozoic basalts in the North China Craton. *Geochimica et Cosmochimica Acta* **72**, 2349–2376.

Mahoney, J., Le Roex, A., Peng, Z., Fisher, R. & Natland, J. H. (1992). Southwestern limits of Indian Ocean ridge mantle

and the origin of low $^{206}Pb/^{204}Pb$ mid-ocean ridge basalt: isotope systematics of the central Southwest Indian Ridge (17°–50°E). *Journal of Geophysical Research* **97**, 19771–19790.

Mahoney, J. J., Nicollet, C. & Dupuy, C. (1991). Madagascar basalts: tracking oceanic and continental sources. *Earth and Planetary Science Letters* **104**, 350–363.

Mahoney, J. J., Saunders, A. D., Storey, M. & Randriamanantenasoa, A. (2008). Geochemistry of the Volcan de l'Androy Basalt–Rhyolite Complex, Madagascar Cretaceous Igneous Province. *Journal of Petrology* **49**, 1069–1096.

Mallick, S., Dick, H. J. B., Sachi-Kocher, A. & Salters, V. J. M. (2014). Isotope and trace element insights into heterogeneity of subridge mantle. *Geochemistry, Geophysics, Geosystems* **15**, 2438–2453.

Meyzen, C. M., Ludden, J. N., Humler, E., Luais, B., Toplis, M. J., Mével, C. & Storey, M. (2005). New insights into the origin and distribution of the DUPAL isotope anomaly in the Indian Ocean mantle from MORB of the Southwest Indian Ridge. *Geochemistry, Geophysics, Geosystems* **6**, Q11K11.

Meyzen, C. M., Blichert-Toft, J., Ludden, J. N., Humler, E., Mével, C. & Albarède, F. (2007). Isotopic portrayal of the Earth's upper mantle flow field. *Nature* **447**, 1069–1074.

Middlemost, E. A. K. (1994). Naming materials in the magma/igneous rock system. *Earth-Science Reviews* **37**, 215–224.

Münker, C., Pfänder, J. A., Weyer, S., Bückl, A., Klein, T. & Mezger, K. (2003). Evolution of planetary cores and the Earth–Moon system from Nb/Ta systematics. *Science* **301**, 84–87.

Nauret, F., Snow, J., Hellebrand, E. & Weis, D. (2011). Geochemical composition of K-rich lavas from the Lena Trough (Arctic Ocean). *Journal of Petrology* **52**, 1185–1206.

Niu, Y. & Batiza, R. (1997). Trace element evidence from seamounts for recycled oceanic crust in the Eastern Pacific mantle. *Earth and Planetary Science Letters* **148**, 471–483.

Niu, Y. & O'Hara, M. J. (2008). Global correlations of ocean ridge basalt chemistry with axial depth: a new perspective. *Journal of Petrology* **49**, 633–664.

Niu, X., Ruan, A., Li, J., Minshull, T. A., Sauter, D., Wu, Z., Qiu, X., Zhao, M., Chen, Y. J. & Singh, S. (2015). Along-axis variation in crustal thickness at the ultraslow spreading Southwest Indian Ridge (50°E) from a wide-angle seismic experiment. *Geochemistry, Geophysics, Geosystems* **16**, 468–485.

Parkinson, I. J. & Pearce, J. A. (1998). Peridotites from the Izu–Bonin–Mariana forearc (ODP Leg 125): evidence for mantle melting and melt–mantle interaction in a supra-subduction zone setting. *Journal of Petrology* **39**, 1577–1618.

Patriat, P. & Segoufin, J. (1988). Reconstruction of the Central Indian Ocean. *Tectonophysics* **155**, 211–234.

Pearce, J. A., Baker, P. E., Harvey, P. K. & Luff, I. W. (1995). Geochemical evidence for subduction fluxes, mantle melting and fractional crystallization beneath the South Sandwich Island Arc. *Journal of Petrology* **36**, 1073–1109.

Pearson, D. G., Irvine, G. J., Ionov, D. A., Boyd, F. R. & Dreibus, G. E. (2004). Re–Os isotope systematics and platinum group element fractionation during mantle melt extraction: a study of massif and xenolith peridotite suites. *Chemical Geology* **208**, 29–59.

Pfänder, J. A., Jung, S., Münker, C., Stracke, A. & Mezger, K. (2012). A possible high Nb/Ta reservoir in the continental lithospheric mantle and consequences on the global Nb budget—Evidence from continental basalts from Central Germany. *Geochimica et Cosmochimica Acta* **77**, 232–251.

Reed, S. J. B. (2005). *Electron Microprobe Analysis and Scanning Electron Microscopy in Geology*. Cambridge: Cambridge University Press.

Rehkämper, M. & Hofmann, A. W. (1997). Recycled ocean crust and sediment in Indian Ocean MORB. *Earth and Planetary Science Letters* **147**, 93–106.

Reid, I. & Jackson, H. R. (1981). Oceanic spreading rate and crustal thickness. *Marine Geophysical Researches* **5**, 165–172.

Salters, J. M. V. & Stracke, A. (2004). Composition of the depleted mantle. Geochemistry Geophysics Geosystems **5**,Q05004, doi:10.1029/2003GC000597.

Salters, V. J. M. & Longhi, J. (1999). Trace element partitioning during the initial stages of melting beneath mid-ocean ridges. *Earth and Planetary Science Letters* **166**, 15–30.

Salters, V. J. M. & White, W. M. (1998). Hf isotope constraints on mantle evolution. *Chemical Geology* **145**, 447–460.

Salters, V. J. M., Longhi, J. E. & Bizimis, M. (2002). Near mantle solidus trace element partitioning at pressures up to 3·4 GPa. *Geochemistry, Geophysics, Geosystems* **3**, 1–23.

Sauter, D., Patriat, P., Rommevaux-Jestin, C., Cannat, M. & Briais, A. (2001). The Southwest Indian Ridge between 49°15′E and 57°E: focused accretion and magma redistribution. *Earth and Planetary Science Letters* **192**, 303–317.

Sauter, D., Mendel, V., Rommevaux-Jestin, C., Parson, L. M., Fujimoto, H., Mével, C., Cannat, M. & Tamaki, K. (2004). Focused magmatism versus amagmatic spreading along the ultra-slow spreading Southwest Indian Ridge: evidence from TOBI side scan sonar imagery. *Geochemistry, Geophysics, Geosystems* **5**, Q10K09.

Sauter, D., Cannat, M., Meyzen, C., Bezos, A., Patriat, P., Humler, E. & Debayle, E. (2009). Propagation of a melting anomaly along the ultraslow Southwest Indian Ridge between 46°E and 52°20′E: interaction with the Crozet hotspot? *Geophysical Journal International* **179**, 687–699.

Sauter, D., Cannat, M., Roumejon, S., Andreani, M., Birot, D., Bronner, A., Brunelli, D., Carlut, J., Delacour, A., Guyader, V., MacLeod, C. J., Manatschal, G., Mendel, V., Menez, B., Pasini, V., Ruellan, E. & Searle, R. (2013). Continuous exhumation of mantle-derived rocks at the Southwest Indian Ridge for 11 million years. *Nature Geoscience* **6**, 314–320.

Shirey, S. B. & Walker, R. J. (1998). The Re–Os isotope system in cosmochemistry and high-temperature geochemistry. *Annual Review of Earth and Planetary Sciences* **26**, 423–500.

Standish, J. J., Dick, H. J. B., Michael, P. J., Melson, W. G. & O'Hearn, T. (2008). MORB generation beneath the ultraslow spreading Southwest Indian Ridge (9–25°E): major element chemistry and the importance of process versus source. *Geochemistry, Geophysics, Geosystems* **9**, Q05004.

Stern, R. J. (1994). Arc assembly and continental collision in the Neoproterozoic East African Orogen: implications for the consolidation of Gondwanaland. *Annual Review of Earth and Planetary Sciences* **22**, 319–351.

Storey, M., Mahoney, J. J. & Saunders, A. D. (1997). Cretaceous basalts in Madagascar and the transition between plume and continental lithosphere mantle sources. In: Mahoney, J. J.& Coffin, M. F. (eds) *Large Igneous Provinces: Continental Oceanic and Planetary Flood Volcanism. American Geophysical Union, Geophysical Monograph* **100**, 95–122.

Stracke, A., Bizimis, M. & Salters, V. J. M. (2003). Recycling oceanic crust: quantitative constraints. *Geochemistry, Geophysics, Geosystems* **4**, 8003.

Straub, S. M. & Zellmer, G. F. (2012). Volcanic arcs as archives of plate tectonic change. *Gondwana Research* **21**, 495–516.

Straub, S. M., Goldstein, S. L., Class, C. & Schmidt, A. (2009). Mid-ocean-ridge basalt of Indian type in the northwest Pacific Ocean basin. *Nature Geoscience* **2**, 286–289.

Straub, S. M., Goldstein, S. L., Class, C., Schmidt, A. & Gomez-Tuena, A. (2010). Slab and mantle controls on the Sr–Nd–Pb–Hf isotope evolution of the post 42 Ma Izu–Bonin volcanic arc. *Journal of Petrology* **51**, 993–1026.

Sun, S. S. & McDonough, W. F. (1989). Chemical and isotopic systematics of oceanic basalts: implications for mantle composition and processes. In: Saunders, A. D.& Norry, M. J. (eds) *Magmatism in the Ocean Basins. Geological Society, London, Special Publications* **42**, 313–345.

Sun, W. (2016). Challenges in solid earth sciences. *Solid Earth Sciences* **1**, 1–4.

Tao, C., Lin, J., Guo, S., Chen, Y. J., Wu, G., Han, X., German, C. R., Yoerger, D. R., Zhou, N., Li, H., Su, X. & Zhu, J. (2012). First active hydrothermal vents on an ultraslow-spreading center: Southwest Indian Ridge. *Geology* **40**, 47–50.

Todt, W, Cliff, RA, Hanser, A, Hofmann, AW, *Evaluation of a 202Pb-205Pb double spike for high precision lead isotope analysis*, Earth Processes: Reading the Isotopic Code, Geophysical Monography Series 95, Basu, AR, Hart, SR,

Torsvik, T. H., Tucker, R. D., Ashwal, L. D., Eide, E. A., Rakotosolofo, N. A. & de Wit, M. J. (1998). Late Cretaceous magmatism in Madagascar: palaeomagnetic evidence for a stationary Marion hotspot. *Earth and Planetary Science Letters* **164**, 221–232.

Wang, J., Zhou, H., Salters, V., Liu, Y., Sachi-Kocher, A. & Dick, H. (2019). Mantle melting variation and refertilization beneath the Dragon Bone amagmatic segment (53°E SWIR): major and trace element compositions of peridotites at ridge flanks. *Lithos* **324–325**, 325–339.

Weyer, S., Münker, C. & Mezger, K. (2003). Nb/Ta, Zr/Hf and REE in the depleted mantle: implications for the differentiation history of the crust–mantle system. *Earth and Planetary Science Letters* **205**, 309–324.

Woodhead, J. D., Hergt, J. M., Davidson, J. P. & Eggins, S. M. (2001). Hafnium isotope evidence for 'conservative' element mobility during subduction zone processes. *Earth and Planetary Science Letters* **192**, 331–346.

Yang, A. Y., Zhao, T.-P., Zhou, M.-F. & Deng, X.-G. (2017). Isotopically enriched N-MORB: a new geochemical signature of off-axis plume–ridge interaction—a case study at 50°28′E, Southwest Indian Ridge. *Journal of Geophysical Research: Solid Earth* **122**, 191–213.

Yang, S., Humayun, M., Righter, K., Jefferson, G., Fields, D. & Irving, A. J. (2015). Siderophile and chalcophile element abundances in shergottites: implications for Martian core formation. *Meteoritics & Planetary Science* **50**, 691–714.

Zhao, M., Qiu, X., Li, J., Sauter, D., Ruan, A., Chen, J., Cannat, M., Singh, S., Zhang, J., Wu, Z. & Niu, X. (2013). Three-dimensional seismic structure of the Dragon Flag oceanic core complex at the ultraslow spreading Southwest Indian Ridge (49°39′E). *Geochemistry, Geophysics, Geosystems* **14**, 4544–4563.

Zhou, H. & Dick, H. J. (2013). Thin crust as evidence for depleted mantle supporting the Marion Rise. *Nature* **494**, 195–201.